COMPUTER AIDED DETECTION OF BRAIN TUMOR USING MAGNETIC RESONANCE IMAGING-MRI

By

NAZISH JAHAN

2009-NUST-MS-CS&E-07

Supervisor

Dr. Khawar Khurshid

NUST-SEECS

Masters in Computational Science and Engineering (MS CS&E)

Research Center for Modeling and Simulation,

National University of Sciences and Technology (NUST),

Islamabad, Pakistan.

(October 2012)

COMPUTER AIDED DETECTION OF BRAIN TUMOR USING MAGNETIC RESONANCE IMAGING-MRI

By

NAZISH JAHAN

2009-NUST-MS-CS&E-07

Supervisor

Dr. Khawar Khurshid

NUST-SEECS

A thesis submitted in partial fulfillment of the requirements for the degree of

Masters in Computational Science and Engineering (MS CS&E)

Research Center for Modeling and Simulation,

National University of Sciences and Technology (NUST),

Islamabad, Pakistan.

(October 2012)

Dedicated to my dear parents,

my sister Kiran and my brother Shahzad

Abstract

Medical image widely use Active contour models (ACMs) or snake for segmentation purposes, specifically to extract tumor boundaries in brain tumor MRI images. ACMs practical applications are limited due to issues related with initialization and weak convergence to boundary concavities. Here comparative study is presented to analyze three different Active contour models (ACMs) of snakes implemented on Brain tumors MR imagery. Where the three ACMs are named as: Gradient Vector Flow (GVF), Boundary vector field (BVF), Generalized Boundary Vector Field (GBVF).

The assessment of results with tumor MR imagery demonstrates that GBVF method is more perfect and robust for brain tumor segmentation. Selected imagery for testing provides difficult and typical problems found in different cross-sectional views of brain tumor MRI segmentation. The comparative results emphasize both the potential and weaknesses of these models.

Table of Contents

Acknowledgments

No piece of work is ever exclusively the product of the individuals whose names appear on its title page. Inevitably, the brainchild of the authors bears the imprint of many forces and people. First of all, I am grateful to Allah Almighty for providing me the opportunity to work in the unique and conductive atmosphere of NUST-RCMS and to give me the strength to complete this thesis.

I am indebted to my advisor, Dr. Khawar Khurshid not only for rendering me his standards of excellence in guiding me throughout the thesis but also for keeping me motivated along the path. What I have achieved holds a huge credit to his guidance.

I am also grateful to my committee members; Dr. Rehan Hafiz, Engr. Sikandar Hayat and Engr. Farooq Cheema. As well as I am highly obliged to Air Cdr. Tahir Mehmood Khalid, for his encouragements and valuable suggestions throughout this thesis.

I am highly indebted to Dr. Irshad Mian (Assistant Professor of Radiology at Sargodha medical college) and Dr. Imran Yusuf (radiologist at Shaukat Khanam memorial, Lahore) who helped me open heartedly during data collection and understanding of medical images.

I want to say special thanks to my classmate Faiz Ali and my friend Iqra Atif for their great support in this journey. The great cooperation I got from my dear parents-in-law, my husband, Zohaib Ahmad, and my family is memorable. Last but not least I would like to thank all my friends, especially Humaira and Shafia, all faculty members and the technical staff of RCMS.

Nazish Jahan.

Chapter 1

1. INTRODUCTION

1.1. Motivation

Now a days, tumor based diseases are among the most serious ailments in the world and their treatment and cure is one of the most prioritized research area in bio-medical engineering. For example, the treatment of Brain cancer is very critical, as the functional system of whole body depends on brain. During surgery, arterial spread areas must be saved in order to avoid medical disorders caused by surgeons. Therefore, it is necessary to give attention to proper diagnosis and treatment planning of such diseases. It is essential that oncologists, neurosurgeons and the whole medical panel should be aware of the knowledge and details of the tumor affected area. Neurosurgeons, oncologists and radiologists prefer brain tumor segmentation from Magnetic Resonance Imaging (MRI) to analyze the tumors responses during treatment. MRI can be useful to plan radiation therapy and to examine the efficiency of new drug. Automatic brain tumor segmentation methods are preferable to manual segmentation as the later is tedious and can be erroneous. The MRI images help in exact diagnosis and treatment planning of the tumor. Therefore, the images play an extremely important role in the assessment of brain tumors and in providing the required knowledge in the usage of the current tools provided by computational

techniques. Thus, benefiting in providing the information recovered from these images during treatment.

Brain tumor is one of the main reasons for the raising of death rate among adults and children. Tumors are the considerable amount of tissues that rise out of regulation of the standard strengths that manage development [1].The complicated brain tumors are divided into two main groups which are dependent on origin of tumors, how severe it is and their growth pattern. Primary brain tumors grow up out of the brain's cells or from the brain's layer. A metastatic or secondary brain tumor arises as a result of cancer cells that expand to the brain out of primary cancer that exists in any other body part. Many researches of progressive countries reflect that a large range of people who are affected by brain tumors are expired as in result has risen possibly about 300 in last thirty years [2].

Detecting the small brain tumors in MRI imagery is more analytically complex than larger tumors, and consequently, increases the risk of human blunder when examined by a consultant. Automatic detection process not only reduce human blunder but also boost the time consuming procedure of assessing large quantity of MRI imagery. Neuro-radiology is perceived as such a field wherein the patient's condition of fitness condition is concluded on the basis of visual examination of imagery obtained through diverse modalities. It entails that the physician's meticulous expertise as well as on the informative data that the clinical group can manage are the factors that play role behind achievement of clinical diagnosis.

Research in this field is exceptionally dynamic. Efforts have been applied to move ahead of the contemporary pixel resolution, and to increase knowledge using "molecular imagery" in magnetic resonance imagery as well as in nuclear medicine. Thus it is proved that imagery is

providing a precious assistance in medical routine. Additionally, several image modalities are utilized often at various time positions; hence it is essential for combining the characteristics exhibited by these distinctive suppliers of imagery. Automatic processing techniques are being advanced enough to appreciate this integration. A number of Computer Aided Diagnostic (CAD) software packages are introduced, specifically to supply supportive analysis in brain cancer, lung, or mammography. These progresses have provoked various clinical treatments.

In image processing of brain tumor, the main objective is the identification of location and expansion of the tumor, i.e. the segmentation of tumor. On the other hand, brain tumors intrinsic destructive actions results ambiguity in the sharpness of neoplastic margins, preventing a precise macroscopic level diagnosis and an exactness of treatment. Analyzing image segmentation at advance level can also produce objective measuring of the related attributes of tumors, like knowledge about metabolic-related information, size or shape, and study of the molecular changes relating to a pathologic performance to a treatment outcome. Regarding to a research the reaction of GBM to chemotherapy can be examined through segmentation of tumor. One more team focused that through image analysis it is realized that the resilience development speed of low-grade gliomas is advantageous to evaluate the threat of conversion of this tumor condition to a malicious one. According to another research heterogeneity-associated brain tumor characteristics have exposed a firm affiliation with the discrimination of a cancerous tumor from a low-grade glioma. Where the presence of edema in white matter has been associated with the tumor severity, differentiating from edema at times can be done through expert's trained eye however it is not easy to identify it mechanically. The above discussed situation, i.e. edema and excessive heterogeneity can be tackled through computational-based techniques, giving uphold to advance the patient supervision.

1.2. Magnetic resonance imaging

High spatial resolution imagery is a mutual characteristic of both Magnetic resonance images (MRI) and computed tomography (CT). As MRI does not involve any contact of ionizing radiation thus it is a secure practice. There are many reasons due to which MRI holds a particular position within imaging modalities. Single machine of MRI can produce a broad range of types of contrast. In addition to effortlessly high-quality soft tissue contrast, its distinctive imaging assembly provides suppleness in slice arrangement at any desired angle in the 3 D space. Despite of the factor that MRI takes more time in inspection than other imaging techniques, the opportunities provided by MRI designate it among the leading imaging mechanisms for neurological research, Image development is consisted of handling of the magnetic attributes of the water hydrogen nucleus, and resulting operation of "tissue magnetization", done in the presence of enough high magnetic field environment. It's a fascinating point that every tissue is rare in its microstructure and possesses distinctive chemical configuration as well as all are different in magnetic characteristics that make them very useful in applications.

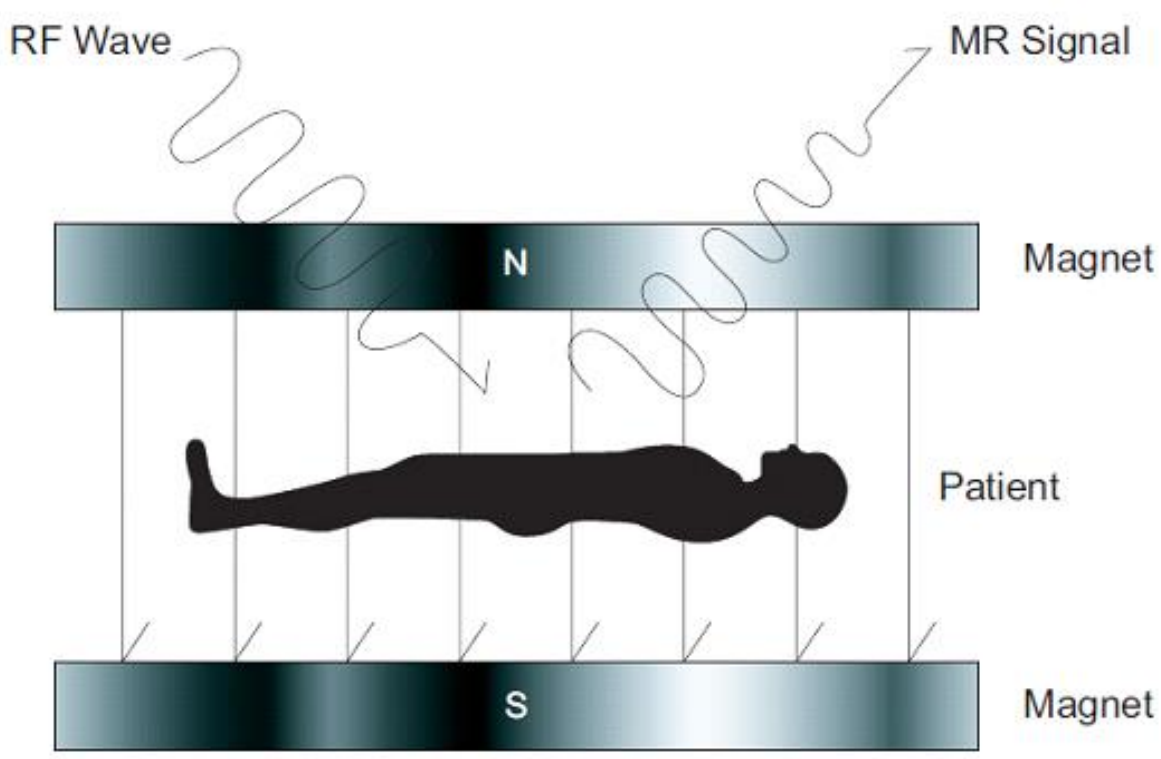

Figure 1.1: Basic set up MRI apparatus

Each tissue possesses unique longitudinal time T1 and transversal relaxation time T2. The Longitudinal relaxation time, T1, represents the duration required by magnetization for retrieval of its original condition; quick magnetization retrieval produces low T1 and high signal.

While time of signal decaying is represented by T2, a smaller T2 means signal decaying is fast and signal is low. T1 and T2 rise due to independent reasons, thus express dissimilar and distinctive tissue uniqueness. A number of methods are used for efficiently dealing tissue magnetization, producing and obtaining MR signal. Due to this support, MRI fundamental contrast types T1- or T2- weighted images are obtainable. Since signal arises within water hydrogen nucleus , overall quantity of signal relies on intensity of water present in tissue and provides third major existing contrast; proton density (PD) weighted images. Efficient choice

of an imaging sequence and proper choice of its parameters are required to obtain the desired contrast type. MR signal is produced as well as controlled on account of sequential usage of some of the factors, namely magnetic field gradient and radiofrequency pulse (RF pulse), with 3 spatial axes. The efficient sequential use of these factors is known as MR sequence. A standard

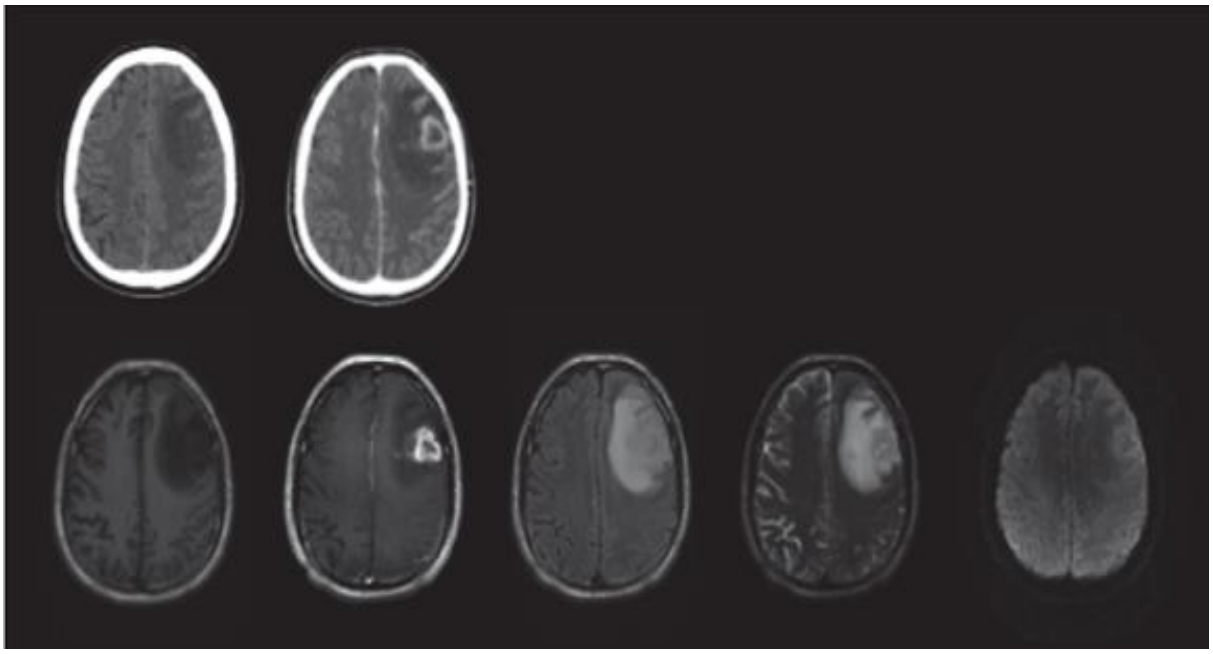

Figure1.2: Glioblastoma Multiforme. Top row: CT images, without CE (left), and with CE (right).Bottom row: MR images. From left to right: T1-weighted, Contrast-Enhanced T1-weighted, FLAIR, and T2-weighted, diffusion-weighted.

MR imaging procedure includes obtaining imagery with various sequences types; selection is done on the basis of desired feature. Usually period of relaxation is greater in brain tumors as compare to normal tissues , well signifies that tumors emerge high intensity on T2-weighted imagery whereas they show low intensity on T1-weighted imagery. However tumors appear as transitional intensities on PD-weighted imagery. The tumor often shows several degrees of cellular solidity and diverse irregularities, visible covering the tumors, like necrosis, hemorrhage, additional fat content, calcification etc.; most brain tumors give assorted look in MR imagery,

like glioblastoma (GBM) exposed in Fig. 1.2. It is difficult to separate out such tumor automatically in precise way as a professional does [4, 5]. Inversion Recovery (IR) sequences are usually used in neurology related purposes. An IR sequence allows signal inhibition from particular tissues on the basis of information of T1, and so presents clear contrast of gray matter–white matter. Fluid Attenuated Inversion Recovery (FLAIR) is proven IR sequence, which represses Cerebrospinal fluid signal and also provides imagery which better differentiate tumor and edema [6].

Contrast agent injection and FLAIR sequences are commonly used together, showing imagery with much difference between background tissues and the tumors. Gadolinium (Gd) chelates is the medium used in MRI for obtaining contrast enhanced imagery, it reduces the T1, and trigger high signal in the organs wherever it reaches. Gd chelates collect in excessive cellular gaps of tumor; similarly like iodine contrast agents behave in CT, as the breaks down of BBB takes place, it provides improved vision of tumors and detailed characterization. Image acquisition post injection and contrast media injection are combined in MR protocols[3, 4]. Fig 1 shows a distinctive ring-like enhancement in surrounding of the tumor

In case of gliomas or metastasis enhancement quality can be improved using high doses of gadolinium. Contrast medium having gadolinium can raise health issues which are being reported by patients especially suffering from kidney dysfunction. Along with gadolinium based contrast further methods are required, particularly to measure tumor proliferation, since enhancement of Gd highly depends on breakdown of BBB. Study shows there are enhancing gliomas which are benign and considerable amount of non-enhancing gliomas are present which are actually malignant in nature. A range of methods are accessible for MR angiography and

perfusion dimensions, such as “Time of Flight” (TOF), or contrast based agent injection ,or “black blood” acquisition and resultant reiterative achievements. Variations of Signal are counted by time and volume. Knowledge about micro vascular system of tumor can be attained, and **it** lets the determination of its level of destructiveness and likely explosion. Magnetic resonance is identified by being a main part of examination, and a lot of applications are now accessible along with T1-, T2-, and PD-weighted imagery.

1.3 Medical Image Analysis

Due to the great development in imaging technology, medical imaging performs progressively more vital part in illustration of the embedded structures of the medical images [6, 7, 8 9]. It is fundamental for biomedical examinations and clinical uses for analysis, surgery or radiotherapy. While modern imaging tools supply significant inspections of internal anatomy, usage of computers for measuring and analyzing large quantity of medical images is restricted. To conform with the requirements, medical image analysis is determined and intends to process, evaluate, and compute embedded structures of medical images accurately, repeatedly, and effectively. Medical image processing and analysis deal with a wide range of research topics.

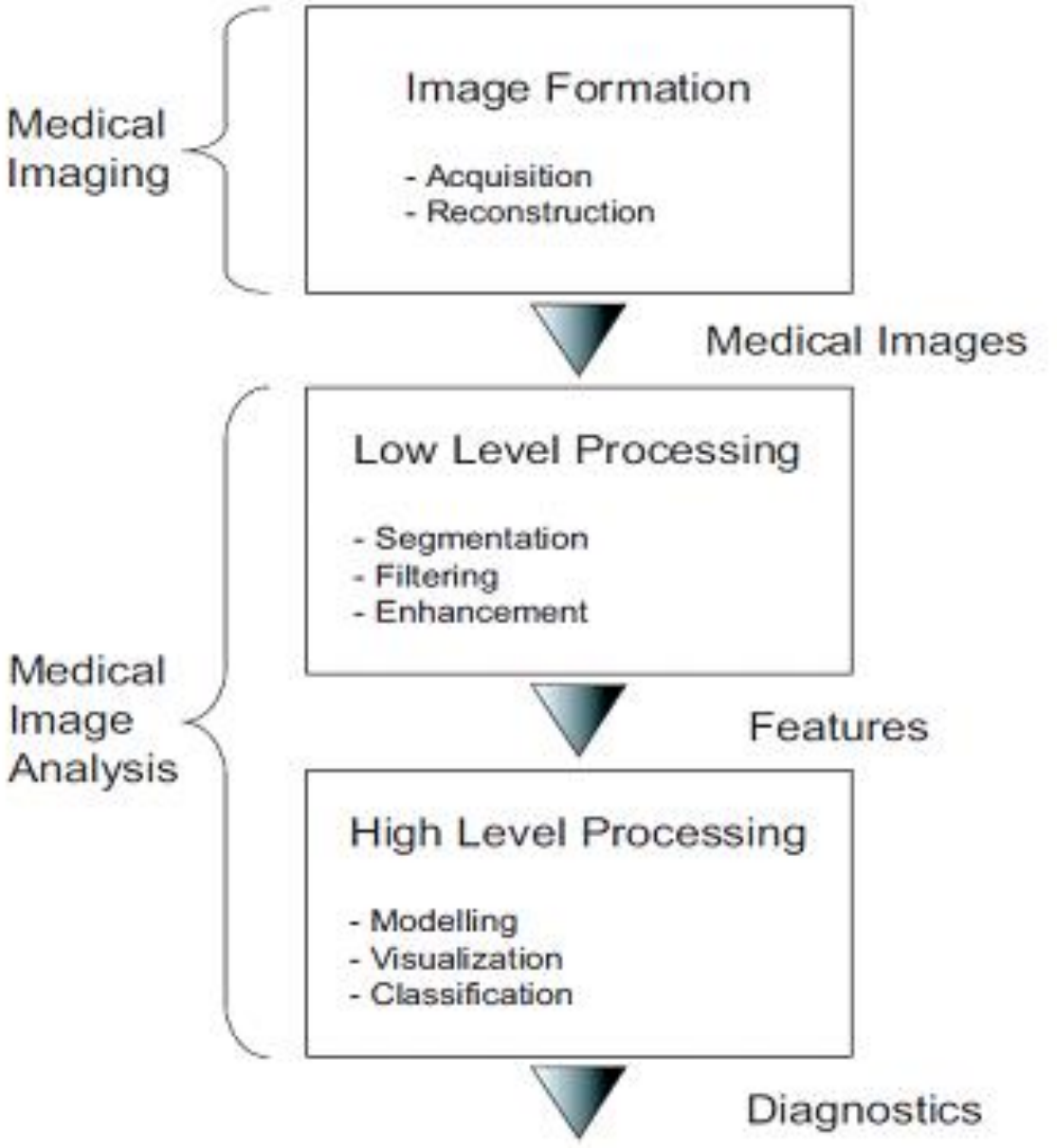

Figure1.3: Structure of Medical Image Analysis

Where several advanced modalities, like CT involve image processing techniques for image reconstruction. Secondly, in medical image analysis, interpretation of the given images is typically done in two phases, first is low level processing and then followed by high level

processing. Features are extracted from raw data set during Low level processing, which involves image preprocessing, segmentation, filtering, or enhancement. The extracted features are used for diagnosis purposes during high level processing. Figure.1.3 shows low level image processing comprises of two basic techniques i.e. image filtering and segmentation, and these are the core steps in medical image analysis. Their accuracies prove the success of the whole diagnostic procedure. Across the last century, the study of image segmentation and filtering has shown considerable improvements. However, they are still the active and continuous research areas since the levels of segmentation and filtering are ill-defined in different applications using different methods.

1.3.1 Image Segmentation

The purpose of segmentation is sectioning an image into panels which are meaningful with respect to a specific application. Every region describes particular type of features, such as, range of intensities, class of textures, kind of shapes, or certain objects. Medical image segmentation is a special example of image segmentation. In clinical practice segmentation is a mean to draw useful embedded anatomies or structures out of an image. Vessel extractions and tumor detections are some of the common practical applications[10]. Image segmentation techniques are generally divided into two major classes, edge based and region based methods.

Region based methods established on collecting together pixel are neighbor as well as share common features, split and mostly obtained by clustering and region growing techniques. Suitable choices of features of interest using region based approach can produce reasonably good regions[11, 12]. Edge based methods based on detecting the image gradient or the strong edges from an image. Edges are actually the disjunction in intensity, color or texture. Similar approach is used by many edge based segmentation techniques. However the usage of edge detection

methods and edge connection methods differentiate them from each other. Using low level image processing procedures like edge detection, mathematical morphology operations, and region growing for segmentation purpose proceeded by manual editing, generally require extensive amounts of expert involvement[11, 12]. Structures boundaries may become vague and detached due to the presence of noises of the acquired medical images, like, spatial aliasing, no uniform illumination and sampling artifacts. These kinds of techniques only consider local information into account hence make it tough to automate these techniques. Consequently, extract information from medical images physicians still depend heavily on tedious manual operations. In this set-up an expert machinist manually marks outs the interested region on every an image volume's slice. There are many severe drawbacks using manual slice editing. However these important performances can be effectively automated through active contour models[12, 13 14]. These methods engage the usage of a sample whose boundary illustration is similar to the image to retrieve the interested object. The contour models approach always assures the development of closed boundary without the requirement of any boundary connection devices. These segmentation techniques begin from an initial curve from manual rough outline. Then the curve is automatically deformed iteratively following some predefined models and rules. The final curves found will then match with the edges of the regions. Active contour models are dynamic and robust research approach to medical image analysis. Shortcomings of basic image processing procedures and physical slice editing can be controlled using active contour model. As well as Segmentation problems reduce with active contour models those are utilizing the prior information about shape of the object and its smoothness. In active contour models boundary of object is considered as a single connected structure. Thus, it not only assure the connectivity and smoothness of an object, but also irregularities, noise, gaps in boundaries of object can be

controlled with this. These properties results in precise and efficient segmentations as well as a profound platform from which to extend automatic analysis methods. Active contour models are proved to be helpful for solving the primary medical image analysis challenges including shape representation segmentation, motion tracking and matching[15, 16, 17].

Segmentation of brain tumors is a complicated job, due to the multifarious anatomy and numerous issues that are built-in into the description of mage. The assorted and diffused pathological description of medical imagery complexes the performance of computational tools intelligent to treat with this vast inconsistency of patterns. Moreover, segmentation techniques can tackle the artifacts and limitations coming with entire image modalities, for example, Magnetic Resonance (MR) imagery is usually despoiled by bias field which is a fluent changing intensity irregularity. Actually it is an un-even intensity pattern, meant for a certain tissue, on an image that is undetectable manually but could be highly observable by an automatic computational method like segmentation.

1.4 Parametric Active Contour

In 1988 parametric active contour model was presented by Kass as snake or active contour. Afterward it has been successfully employed in various problems of medical image analysis and computer vision, such as motion tracking, edge and subjective contours detection and segmentation. Snakes have proved practically valuable in medical image segmentations. Some of the examples are lung segmentation from magnetic resonance images, automated analysis of nerve cell images and detection of rolling leukocyte within intra-vital microscopy .The key benefit of snake models, as compare to traditional edge detection approaches is that they include image and spatial information in extraction of smooth border of the ROI region of interest[2, 3, 4]. An initial rough approximation of the desired border is defined and the curve deforms to attain the final best possible shape. Hence, isolated artifacts are not counted when they intrude

with the smoothness of the curve. Snake is actually an elastic curve as seen in Fig. 1.4, which is composed of connected nodes.

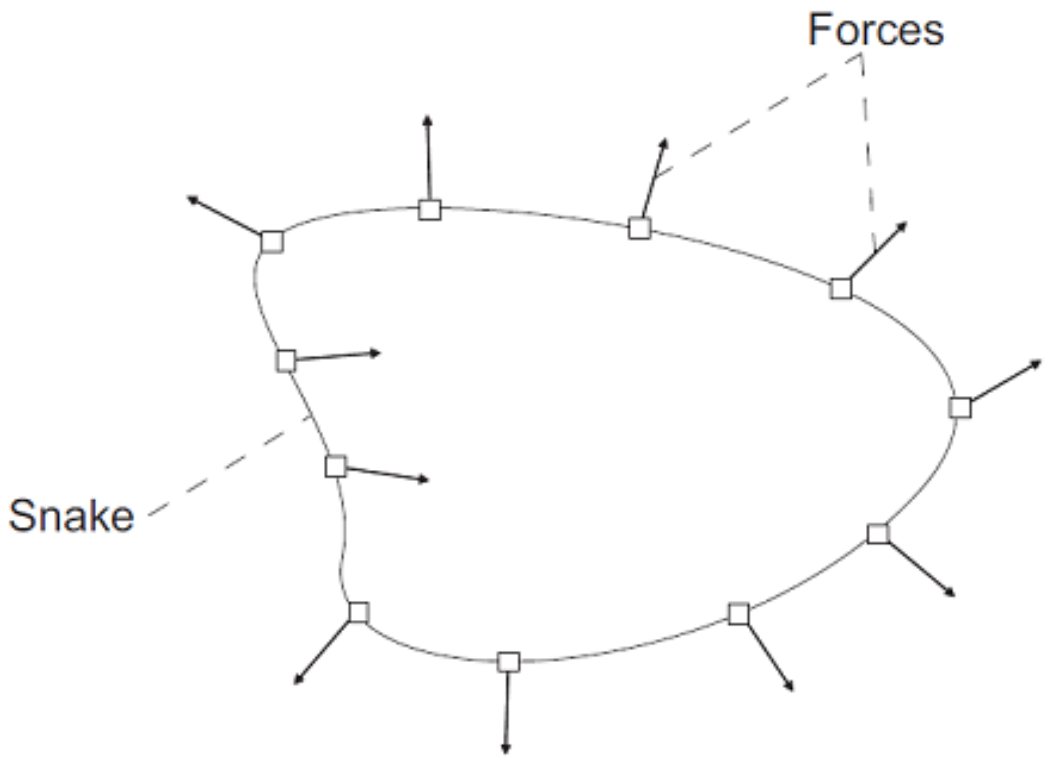

Figure1.4: Elastic nature of snake.

The logic behind this name active is that it can dynamically adjust to object shapes by reducing a defined energy functional iteratively. The functional comprises of internal forces and external forces, due to mathematical formulation it becomes simpler to combine in a single deformation process, all those of an initial approximated required are properties of contour, information dependent constraints and image data.

$$J(c) = \int_0^1 F_{int}\big(c(s)\big) + F_{ext}\big(c(s)\big)\, ds$$

Where F_{int} the internal force and F_{ext} is the external force, while s refers to the node indexes of the snake and keep in the range of [0; 1].one of the first uses of active contour in medical image analysis was the segmentation using snakes for both 2D and 3D data sets.

In some cases Snake models have their own natures or limitations. First, as it is assembled by a pre-defined curve, it was meant to deal topologically simple objects. Since without using extra machinery the topological changes cannot be handle through mathematical model. Thus topological structures required to be identified in prior. However, this is beneficial in some situations if it is employed for topologically simple objects against complex background. It is handled easily and prevents over-segmentation with not inevitable topological changes. Secondly contraction force of internal energy term and concavity of the energy functional make the parametric snakes significant to their preliminary conditions. Thus, development of effective external term is essential for snake model to be successfully applicable in practical applications.

Chapter 2

METHODOLOGY

2.1 Introduction

Image processing has extensively utilized Active contour models in various applications. Basically, active contours are divided into two main categories i.e. first is parametric active contours and the second is geometric active contours. Here the focus is on the development of parametric active contours. Snake structure is characterized clearly like parameterized curves. Primitively established by Kass et al. [14] the snake model has been now developed into various snake models, utilized by many forms of images for practical applications like image tracking and image segmentation Parametric active contours evolve the closed or open curves under the dominancy of forces generated by external and internal energy terms. The purpose of development of most of these forces was to either regulate the framework of snake or improvement in extraction process of object boundary. Bending force and elasticity force are examples of internal forces. Where image gradient, distance potential force, balloon and pressure are some of the examples of external forces. While implementing the traditional snakes, requirement is to place the original snake carefully in the vicinity of target object, else due to limited capture range it will attract towards the local minima. Snake improved its capture range through the distance potential force which was characterized on the basis of Euclidian distance. However just like behavior of traditional snakes, the snake with distance potential force cannot grow onto concavity.

Then Gradient vector flow (GVF) was developed in order to boost the snake potential to drive into the concavities [15]. In coming time this development brought remarkable advancements in snake models. Various novel snake models were proposed by merging diverse methods into GVF snake. However, in GVF snake model, limitation of capture range is still a problem and its execution is a computationally heavy procedure. GVF snake spreads the gradient data starting at the object boundary to the other

portions of the image that results in extension of capture range. Non-linear diffusion method was applied to handle this shortcoming of GVF snake, but, intensive computation still remained a problem.

2.2 Two Dimensional Traditional Snake

The basic 2-D snake has a curve shaped structure

$$X(s) = [x(s), y(s)], \qquad s \in [0,1]$$

For reducing an energy function, the snake grows via image's spatial region.

$$E = \int_0^1 \left[E_{int}\big(x(s)\big) + E_{ext}\big(x(s)\big)\right] ds \qquad (2.1)$$

E_{int} is a term for internal force, and E_{ext} is a term for external force. The internal energy function is meant to impose a shape on the deformable contour and to preserve an even distance between the points in the contour

$$E_{int} = \int_0^1 \frac{1}{2}\left(\alpha\left|x'(s)\right|^2 + \beta|x''(s)|^2\right) ds$$

stress and tension of snake are handled by weighting parameters α and β. Where $x'(s)$ indicates the first and $x''(s)$ indicates second derivatives of *x(s)* regarding *s*. E_{ext} the external force is obtained out of the image that is why possessing smaller numerical values at the characteristics of interest, like boundaries. Assumed *I(x, y)* a gray-level image, considered as a function of variables *(x, y)* having continuous position. A basic external force developed to direct a snake for step edges are

$$E_{ext}^{(1)}(x,y) = -|\nabla I(x,y)|^2 \qquad (2.2)$$

$$E_{ext}^{(2)}(x,y) = -|\nabla(\mathrm{G}_\sigma(\mathrm{x},\mathrm{y}) * I(x,y)|^2 \qquad (2.3)$$

Where $G_\sigma(x, y)$ reprents 2 dimensional Gaussian function having standard deviation σ and gradient operator ∇ . For binary image suitable external forces comprise of

$$E_{ext}^{(3)}(x, y) = I(x, y) \qquad (2.4)$$

$$E_{ext}^{(4)}(x, y) = G_\sigma(x, y) * I(x, y) \qquad (2.5)$$

These definitions show that higher value of σ´s forms the edges blurry. However in snake model large values of σ´s are frequently required for enhancing its capture range. Initial snake that reduces *E* should meet the requirements of Euler equation

$$\alpha x''(s) - \beta x'''(s) - \nabla E_{ext} = 0 \qquad (2.6)$$

That can be analyzed by force balance equation

$$F_{int} + F_{ext}^{(p)} = 0 \qquad (2.7)$$

Where

$$F_{int} = \alpha x''(s) - \beta x'''''(s)$$

and

$$F_{ext}^{(p)} = -\nabla E_{ext}$$

F_{int} suppresses the tension and bending where $F_{ext}^{(p)}$ drag the snake in direction of the interested image edges. In order to search the solution to (2.6), the snake is made active by dealing such that *x* is dependent on time *t* in addition to $s(s, t)$. And so, partial derivative of *x* regarding *s* is put equivalent to the left side of (2.6) as shown below

$$x_t(s, t) = \alpha x''(s, t) - \beta x'''(s, t) - \nabla E_{ext} \qquad (2.8)$$

As the result $x(s, t)$ becomes stable, the term $x_t(s, t)$ disappears and a solution of (2.6) will accomplish. Discretize the equation and execute the discrete system repeatedly so numerical result to (2.8) can be determined. It is notable that a lot of snake implementations seek the factor, either it multiplies x_t to

manage the step-size according to time, or it multiplies ∇E_{ext}, which allows independent influence of the external force strength. The traditional snake model shows that evolution of snake highly depends on the external force. Using typical external force in (2.3), results in evolution of the snake in conformity with blurred edges. Increase in standard deviation of the Gaussian function enhance the capture range of the snake, however the boundary localization turns lesser in accuracy and sharpness. In case of traditional snake the capture range is limited, so it is necessary to carefully initialize the snake in vicinity of the target boundary.

2.3 GVF Deformable Contours

The idea behind GVF was to design to a snake taking dynamic force equation (2.8) as an initial point [15]. So the potential force -∇E_{ext} in (2.8) replaced with v(x) as follow

$$X_t(s,t) = \alpha\, x''(s,t) - \beta x''''(s,t) + v(x) \qquad (2.9)$$

Its numerical solution is obtained by discretizing the equation and solving it iteratively, in the same manner as traditional snake. While the ultimate design of GVF snake assures force-balance equation (2.7), Euler equations of the energy minimization problem (2.1) is not characterized by this equation as $v(x)$ generally does not use on account of negative gradient of a potential function. The failure of such desirable property, though, is well-balanced by the considerably better functioning of GVF snake.

2.3.1 Edge Map

Image I(x) deduce *edge map f(x)* which has the attributes that its value is bigger close to the image edges. Gray-level or binary edge map can be used such as

$$f(x) = -E_{ext}^{(i)}(x) \qquad (2.10)$$

The value of i is 1 to 4. Generally edge maps have three attributes that are significant in the current situation. Firstly, edge map has the gradient ∇f that has vectors pointing in the direction of the edges. Secondly, the vectors produced generally show big magnitudes just in close surrounding area of edges.

Thirdly, *I(x)* remains almost invariant in the homogeneous areas so ∇f is just zero. Here the external force is formed using edge map gradient. Due to first property, the snake defined nearby the edge will come to a steady arrangement in close proximity to the edge. It is a well inevitable desirable property. Normally the effect of second property is that it will produce the capture range i.e. not large enough. Third property does not generate any external force at homogeneous regions. Second and third properties are not required. Goal of GVF model is to hold the extremely attractive property of the gradients close to the edges. However it uses a computational diffusion process to enhance the gradient map at a greater extent starting near the edges and spread to homogeneous areas. An important advantage come out of the inbuilt struggle of diffusion procedure will also produce vectors those direct towards concave regions.[8]

2.3.2 Gradient Vector Flow

GVF was the external force proposed in [25] to move the snake through concavities. GVF field v(x) is like stability solution to the underlying vector diffusion formula

$$u_t = g(|\nabla f|)\nabla^2 u - h(|\nabla f|)(u - \nabla f) \qquad (2.11a)$$

$$u(x, 0) = \nabla f(x) \qquad (2.11b)$$

In Eq. (2.11a), the first expression is the *smoothing term* as this expression alone generates easily changing vector field. In Eq. (2.11a), the other expression is the *data term* as it supports **u** vector field to get nearer to ∇f calculated out of the data. *g(.)* is the coefficient of smoothing expression and *h(.)*is the coefficient of data expression. As these coefficients rely on the edge map gradient which is spatially changing, that's why coefficients are spatially changing, As it was required for vector field **u** to be gradually-changing at distant positions of edges [16], but to be adjust to Δf nearby the edges, where *g(.)* and *h(.)* must be consistently neither increasing nor decreasing functions of $|\nabla f|$, in that given order.

$$g(|\nabla f|) = \mu \qquad (2.12a)$$

$$h(|\nabla f|) = |\nabla f|^2 \qquad (2.12b)$$

As $g(.)$ is constant, smoothing found all over; but, $h(.)$ develop high in close proximity to sharp edges, so becomes significant on the boundaries. Therefore, good edge localization should be provided by GVF that is computed using such weighting factors. When there are two edges in close vicinity like a stretched thin cavity next to the boundary, the smoothing effects becomes prominent. At this moment, GVF leans to flat the opposite edges, weakening the energies compulsory to push snake into this area. To tackle this difficulty, weighting functions were proposed in which $g(.)$turns into smaller as $h(.)$stretch outs larger. Then there will be very small smoothing in the vicinity of large gradients, and the effective vector field will be almost equivalent to edge map's gradient.

$$g(|\nabla f|) = e^{-(\frac{|\nabla f|}{k})^2} \qquad (2.13a)$$

$$h(|\nabla f|) = 1 - g(|\nabla f|) \qquad (2.13b)$$

The GVF field processed with these weighting functions adapted the edge map gradient at sharp edges. However it will deviate gradually aside by the boundaries. Degree of swapping among smoothness of field and conformity of gradient can be determined to some extent through the specification of *k*.

GVF is defined by vector diffusion equation (2.11) with a range of weighting functions that will be executed by applying an explicit finite difference method. It will result in steady state when the time step Δt and the spatial sample spaces $\nabla x \; and \; \nabla y$ fulfill

$$\Delta t \leq \frac{\Delta x \, \Delta y}{4 \, g_{max}}$$

Here g_{max} is the greatest quantity of $g(.)$ across the extent of gradients found in edge map of the image.

2.4 Boundary Vector Field

2.4.1 Boundary Map

Grey-level image is composed of a matrix, I(x; y). On the basis of typical external force (2.3) boundary map is defined and re-write as follows:

$$F_B(x, y) = -|\nabla[G_\sigma(x, y) * I(x, y)]|^2 \qquad (2.14)$$

Then boundary map is normalized and a threshold (i.e. T 2 [0; 1]) is applied to convert it into binary map. It will be decided by binary boundary map that which pixels of the image are boundary points which are non-boundary points.

2.4.2 Potential Functions

Two potential functions Ψ_x and Ψ_y are generated independently as result of applying interpolations line-by-line in two scans of binary boundary map. They are horizontal and vertical directional as shown below.

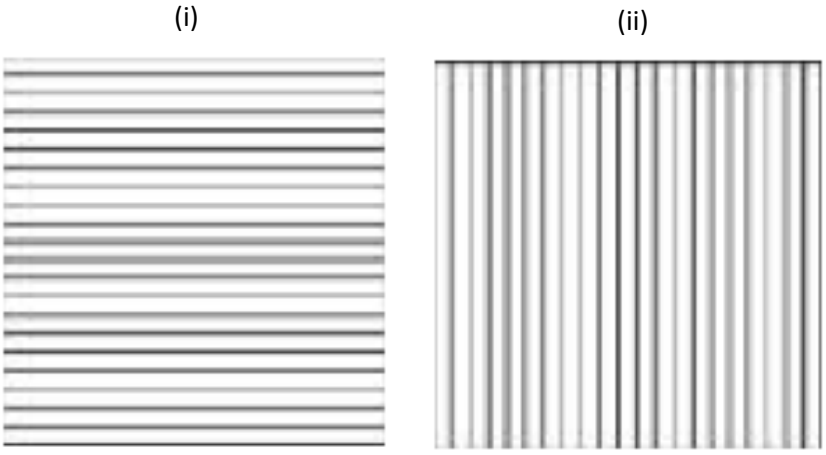

Figure 2.1: Scanning lines of interpolation: (i) Horizontal; (ii) Vertical

Object boundary B_O and image boundary B_I are the boundary points used during interpolations. B_O is characterized by boundary points shown in binary boundary map. The values obtained after normalization of boundary map are assigned to its potential function. The BI is characterized by the broadened boundary of the image where it is assigned zero potential value. Their potential values are set as shown below:

$$\Psi(x,y) = \begin{cases} F_B(x,y) & , \quad (x,y)\epsilon B_O \\ 0 & , \quad (x,y)\epsilon B_I \end{cases} \tag{2.15}$$

Now potential values are assigned to the non-boundary points computing interpolations. Entire non-boundary points exist between B_I or B_O points in either of three settings, independent of scanning directions.

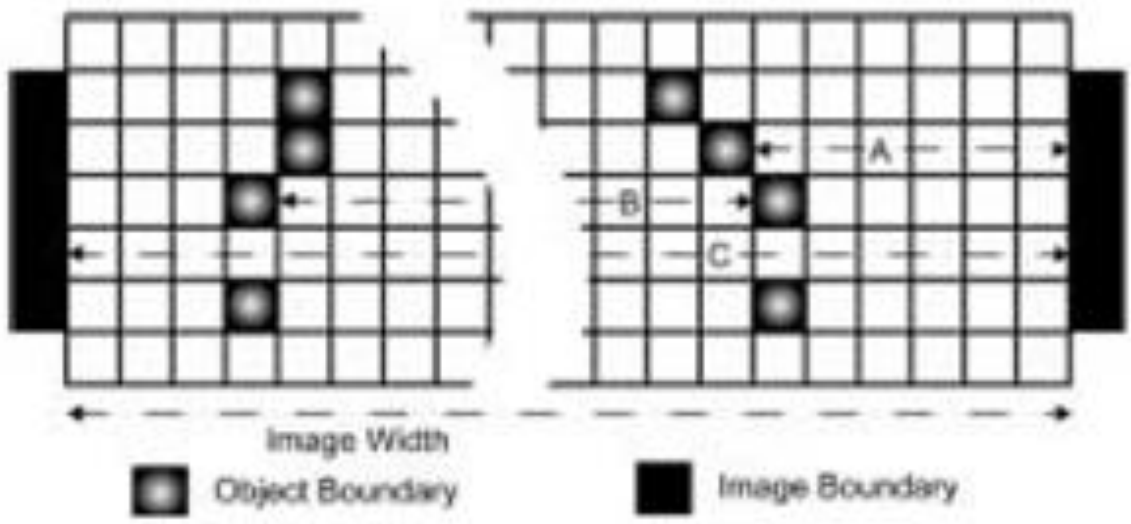

Figure2.2: Three interpolation scenarios, area A is bounded by both object and image boundaries, area B is bounded by two object boundaries, and area C

For the points that are being captured between object boundary and image boundary, their potential values are calculated through linear interpolation [16]

$$\Psi(x, y) = (1 - \delta)\Psi(x_{o,}y_o) + \delta\Psi(x_{i,}y_i) \qquad (2.16)$$

Where bounding object coordinates are $(x_{o,}y_o)$and image boundary coordinates are$(x_{i,}y_i)$. The point is moved from one boundary to next boundary using step size $\delta\epsilon$ [0, 1]

The points that are not part of above situation, they are captured between two object-boundaries otherwise by two image-boundaries. Such situations, do not allow simple linear interpolation due to the identical

potential values posses by confining boundary points. Thus, defined basis functions includes unit interval as shown:

$$\theta_1 = \begin{cases} 1-\delta & , \quad \delta \in [0,1] \\ 0 & , \quad \delta \notin [0,1] \end{cases} \qquad (2.17)$$

$$\theta_2 = \begin{cases} \delta & , \quad \delta \in [0,1] \\ 0 & , \quad \delta \notin [0,1] \end{cases} \qquad (2.18)$$

or the points captured between two object boundaries, represented by B_O1 and B_O2. These points are located at $(x_{o1,}y_{o1})$ and $(x_{o2}y_{o2})$ and their potential values are calculated as under:

$$\Psi(x,y) = \theta_1\left(\frac{(x,y)-(x_{o1,}y_{o1})}{(x_m,y_m)-(x_{o1,}y_{o1})}\right) + \theta_2\left(\frac{(x,y)-(x_{o1,}y_{o1})}{(x_{o2}y_{o2})-(x_m,y_m)}\right) \qquad (2.19)$$

Where (x_m,y_m) is a middle position connecting $(x_{o1,}y_{o1})$ and $(x_{o2}y_{o2})$. the middle position is inserted with the intention of including non-linearity in basic linear potential function[17]. Potential values for the points captured between image boundaries represented as B_I1 and B_I2, which are located at $((x_{I1},y_{I1})$ and $(x_{i2,}y_{i2})$, s calculated using following formula:

$$\Psi(x,y) = \omega\left[\theta_2\left(\frac{(x,y)-(x_{i1,}y_{i1})}{(x_m,y_m)-(x_{i1,}y_{i1})}\right)\right] + \left[\theta_1\left(\frac{(x,y)-(x_m,y_m)}{(x_{i2,}y_{i2})-(x_m,y_m)}\right)\right] \qquad (2.20)$$

Where (x_m,y_m) is the middle position of points which are located at $(x_{i1,}y_{i1})$ and $(x_{i2,}y_{i2})$, where a positive value is normally assigned to weighting factor ω.

2.4.3 Boundary Vector Field

Potential functions' gradients give rise to the formation of two 2-D boundary vector fields (BVF) as discuss below

$$\Phi_{1} = \left[\nabla\Psi_{x,} \nabla\Psi_{y,} \right] \qquad (2.21)$$

Potential functions of both horizontal as well as vertical are involved in BVF1, Φ_1 , like shown above. The BVF1 execution is quite easy, potential functions involves two scans during producing and no repeated optimization method is demanded.

2.5 Generalized boundary vector field GBVF

Four potential functions $\Psi_{x,}$,Ψ_{y},$\Psi_{xy,}$ and Ψ_{yx} are generated independently as result of applying line by line interpolations into four individual scans of binary boundary map. The patterns of these scans are (a) horizontal, (b) vertical, and (c) two diagonal directions as depicted below.

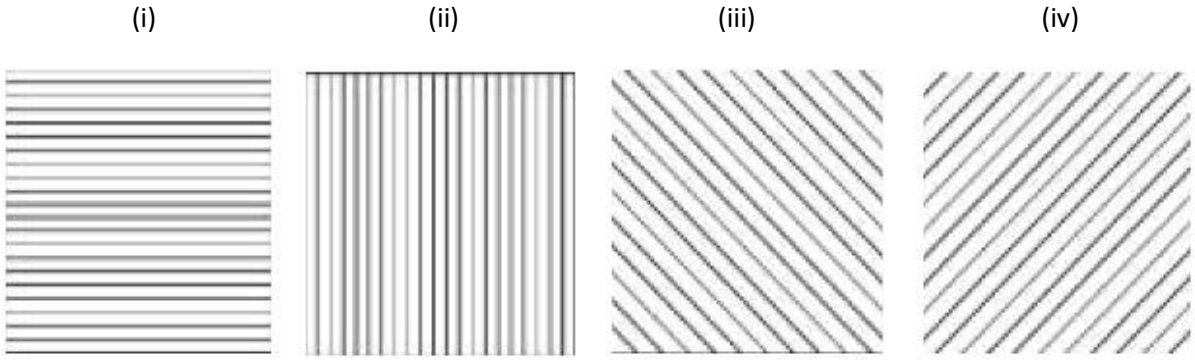

Figure 2.3: Scanning lines of interpolation: (i) Horizontal; (ii) Vertical; (iii) and (iv) Diagonal

Boundary points used during interpolations are of two kinds: (i) object boundary B_O and (ii) image boundary B_I. B_O is characterized as the boundary points shown in the binary boundary map. The values obtained after normalization of boundary map are assigned to its potential function. The B_I is characterized by the broadened boundary of the image where it is assigned zero potential value. Their potential values are set as shown below:

$$\Psi(x,y) = \begin{cases} F_B(x,y) & , \quad (x,y)\epsilon B_O \\ 0 & , \quad (x,y)\epsilon B_I \end{cases}$$

Now potential values are assigned to the non-boundary points computing interpolations. Entire non-boundary points exist between B_I or B_O points in either of three settings, independent of scanning directions.

For the points that are being captured between object boundary and image boundary, their potential values are calculated through linear interpolation

$$\Psi(x,y) = (1-\delta)\Psi(x_{o,}y_o) + \delta\Psi(x_{i,}y_i)$$

Where bounding object coordinates are $(x_{o,}y_o)$ and image boundary coordinates are $(x_{i,}y_i)$. The point is moved from one boundary to next boundary using step size $\delta\epsilon$ [0, 1]

The points that are not part of above situation, they are captured between two object-boundaries otherwise by two image-boundaries. Such situations, do not allow simple linear interpolation due to the identical potential values posses by confining boundary points[18]. Thus, defined basis functions includes unit interval as shown:

$$\theta_1 = \begin{cases} 1-\delta & , \quad \delta \in [0,1] \\ 0 & , \quad \delta \notin [0,1] \end{cases}$$

$$\theta_2 = \begin{cases} \delta & , \quad \delta \in [0,1] \\ 0 & , \quad \delta \notin [0,1] \end{cases}$$

For the points captured between two object boundaries, represented by $B_O 1$ and $B_O 2$. These object boundaries are located at $(x_{o1,} y_{o1})$ and $(x_{o2} y_{o2})$ and their potential values are calculated as under:

$$\Psi(x,y) = \theta_1 \left(\frac{(x,y) - (x_{o1,} y_{o1})}{(x_m, y_m) - (x_{o1,} y_{o1})} \right) + \theta_2 \left(\frac{(x,y) - (x_{o1,} y_{o1})}{(x_{o2} y_{o2}) - (x_m, y_m)} \right)$$

Where (x_m, y_m) is a middle position connecting $(x_{o1,} y_{o1})$ and$(x_{o2} y_{o2})$. The middle position is inserted with the intention of including non-linearity in basic linear potential function. Potential values for the points captured between image boundaries represented as $B_I 1$ and $B_I 2$, which are located at (x_{i1}, y_{i1}) and $(x_{i2,} y_{i2})$, is calculated using following formula:

$$\Psi(x,y) = \omega \left[\theta_2 \left(\frac{(x,y) - (x_{i1,} y_{i1})}{(x_m, y_m) - (x_{i1,} y_{i1})} \right) \right] + \left[\theta_1 \left(\frac{(x,y) - (x_m, y_m)}{(x_{i2,} y_{i2}) - (x_m, y_m)} \right) \right]$$

Where (x_m, y_m) is the middle position of points which are located at $(x_{i1,} y_{i1})$ and $(x_{i2,} y_{i2})$, and a positive value is normally assigned to weighting factor ω.

Generalized Boundary Vector Field

Potential functions' gradients give rise to the formation of two 2-D boundary vector fields (BVF) as discuss below

$$\Phi_1 = \left[\nabla \Psi_{x,} \nabla \Psi_{y,} \right]$$

$$\Phi_2 = \left[\frac{1}{\sqrt{2}} \left(\nabla \Psi_{xy} + \nabla \Psi_{yx} \right), \frac{1}{\sqrt{2}} \left(\nabla \Psi_{xy} + \nabla \Psi_{yx} \right) \right] \qquad (2.22)$$

Potential functions of both horizontal as well as vertical are involved in BVF1, Φ_1 and Potential functions of both of the diagonal directions are involved in BVF2, Φ_2 like shown above. The BVF1 execution is

quite easy, potential functions involves two scans during producing and no repeated optimization method is demanded.

GBVF snake, is defined based on the traditional snake in (1) by applying two BVFs one by one as the external force:

$$E_{ext}(x, y) = \Phi(x, y)$$

Initially BVF1 is applied and evolves the snake until it converges. Later BVF2 is applied and snake evolves until it reaches to the final destination. Computation required for GBVF is quite uncomplicated and comprises of just four scans to produce potential functions. There is no need of any repeated optimization method [17].

2.6. Computational setup

Testing is done with the purpose to present perception of the potency and limitation of the three ACMs using for applications involves segmentation of brain tumor MR images. Testing series with the common objections created by this imagery are presented in Sec: 2.3.1. Where execution specification of the parameter assignment, adjustment, and testing with more types of snake initialization are covered in Section 2.8

2.3.1. Image test set

Demonstrative test set is based on a series of fourteen 2D images which are chosen to show the performance as shown in Fig.2 1. Every tested image is one out of numerous same imagery slices present in given catalog. The collection comprises of interpretation of MRI. Here Head at different cross-sectional views is presented as the biomedical material. Different resolutions and sizes of test images are used. The entire test images used 0–255 range of gray levels. Sharp edges close to the scarce edge, weak or blur edge; heterogeneous internal intensity distribution and

complicated shaped tumors with concavities are common complexities of image processing existed in test set and are a few of the common issues that could disappoint any regular segmentation techniques. The ACM results were compared with manual contours i.e. a ‘‘ground truth’’ segmented by radiologist pixel-by-pixel and were exposed with yellow color on the testing imagery. Excluding the knowledge of the done segmentation procedures, the same radiologist intuitively graded the computerized outcomes to give a quality based judgment.

2.7 Implementation and experimental settings

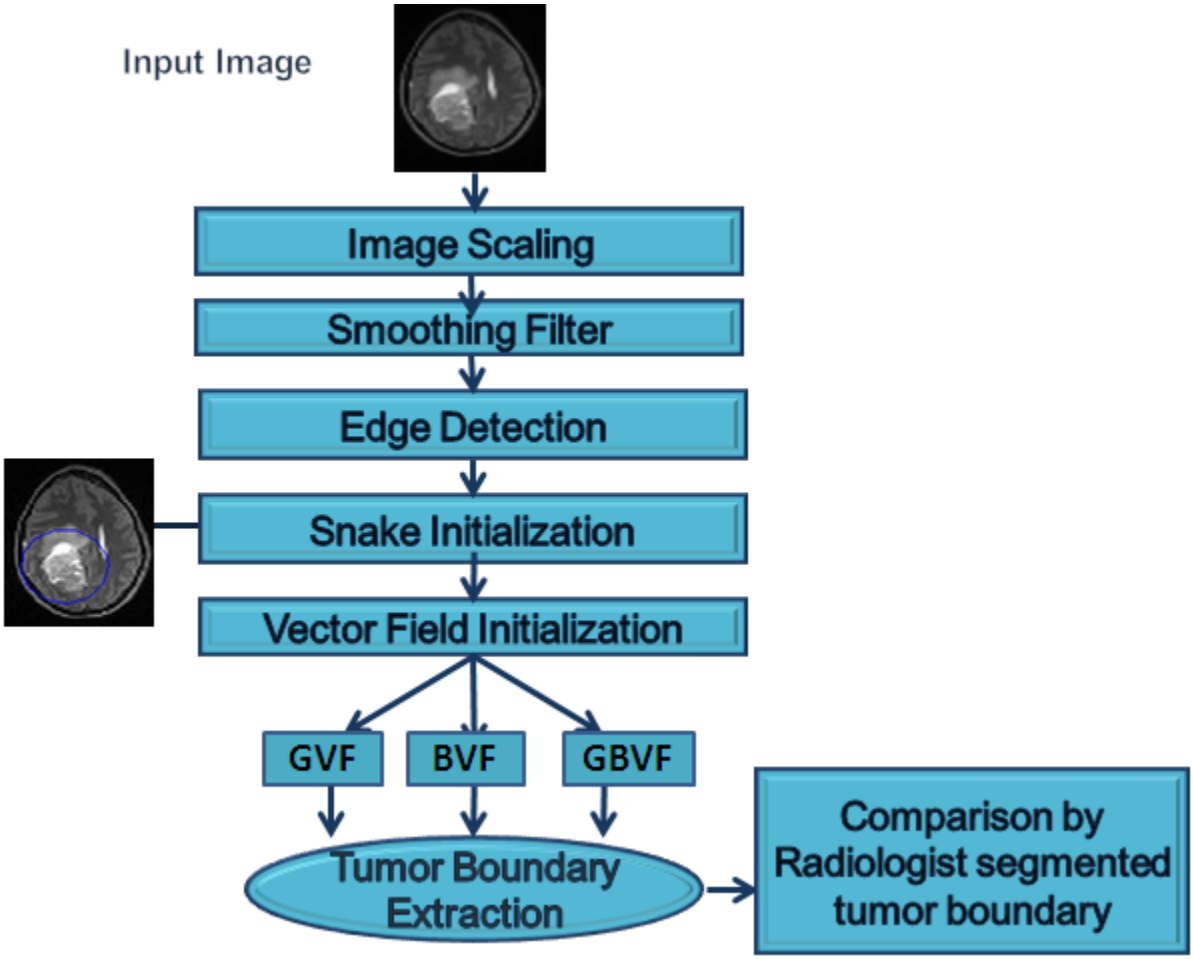

Recognition of all the flexible parameters was initial step in execution of all three models. For each model a computational program was built in Matlab. Scaling is done to (ex. 256 · 256). The

three ACM under observation possessed some common simple features: The single Pre-processing carried out on the imagery was Gaussian ($5 \cdot 5$, σ 1) blur filtering. Edge maps were formed using the gradient magnitude of imagery otherwise their threshold findings of the Gaussian blurred images; A circular shaped ($3 \cdot 3$) initial contour originated on the starting location, an interested image point was chosen by the user; no earlier knowledge of the object shape was utilized. The parameters, in each group of ACM, are very alike and are explained in the coming section. The parameter assignment and adjustment procedure for all three models is described as under.

2.7.1 Parameters

The ACMs possesses some mutual parameters: rigidity (r), elasticity (e), deformation step (ds), external force (x) and viscosity (v). In the traditional snake model in equation (2.1) the e and r parameters are related to internal force varying factors α and β. To iteratively modifying contour position v and ds parameters are applied, but implicitly involve within deformation-equations. Throughout the deformation process smoothness of the contour was preserved through the composition of the e and r parameters. The deforming contour will produce self-intersections and corners by reducing e or r, where raising these parameters excessively will contract that contour to single point or line[22, 23]. To modify the contour location v the influenced parameter employed to regulate the viscosity. Deformation procedure of contour will be delayed by rising value of v and results in more steady deformation. During iterations, the v was restricted to lesser than 15 to prevent a big deformation step. Where the potency of effecting of the image characteristic that form external force is dependent on x that was influential variable. The highest amount of deformations that were allowed was assigned by DS parameter.

2.8 Snake initializations

Around the user elected place, we can found the initial contour as circle shaped, included twice deviations of initial contour sizes and positions, as shown in (figures). In that computational work, the initial contours were estimated as adjoining the entity and circle crossing the final tumor boundary. The contours either expanded or contracted to approach the tumor boundary [24]. The method explained in the earlier section was used to define the parameter setting and tuning process for this numerical code. The main objective of the code was to check the sensitivity of the ACMs on different initial conditions.

2.8.1 Different snake initializations

Furthermore, in medical imagery techniques initial contours for ACMs segmentations can be introduced by (1) inserting an outsized circle out of preferred boundary (2) outline a rough estimated circular boundary partly cover the required object (3) inserting a tiny contour inside the object. The main calculation concentrated on the third part (3) because it demands the lowest degree of user contact for programmed image segmentation. Two other initializations, (1) and (2), were employed to demonstrate the effect of the ACMs. As described in Section 3.3.3.

In order to explain these dissimilar initial conditions, an exemplary image was collected. For these test cases the restrained optimization technique was not to be used because that demands the initial contour being placed inside the object. GVF snakes could appropriately find some portions of the object boundary whenever initial contour was inside the object, and there was no objects partly cover at these object segments [25, 26]. And when the initial contour is at exterior of the object and they were nearer to the edges of the neighboring objects than those of the desired object so they were attracted to edges of other objects. It can be expected the GVF snakes

will be pulled towards interested boundary, when the adjacent region of the object is clean with no other objects.

Chapter 3

RESULTS

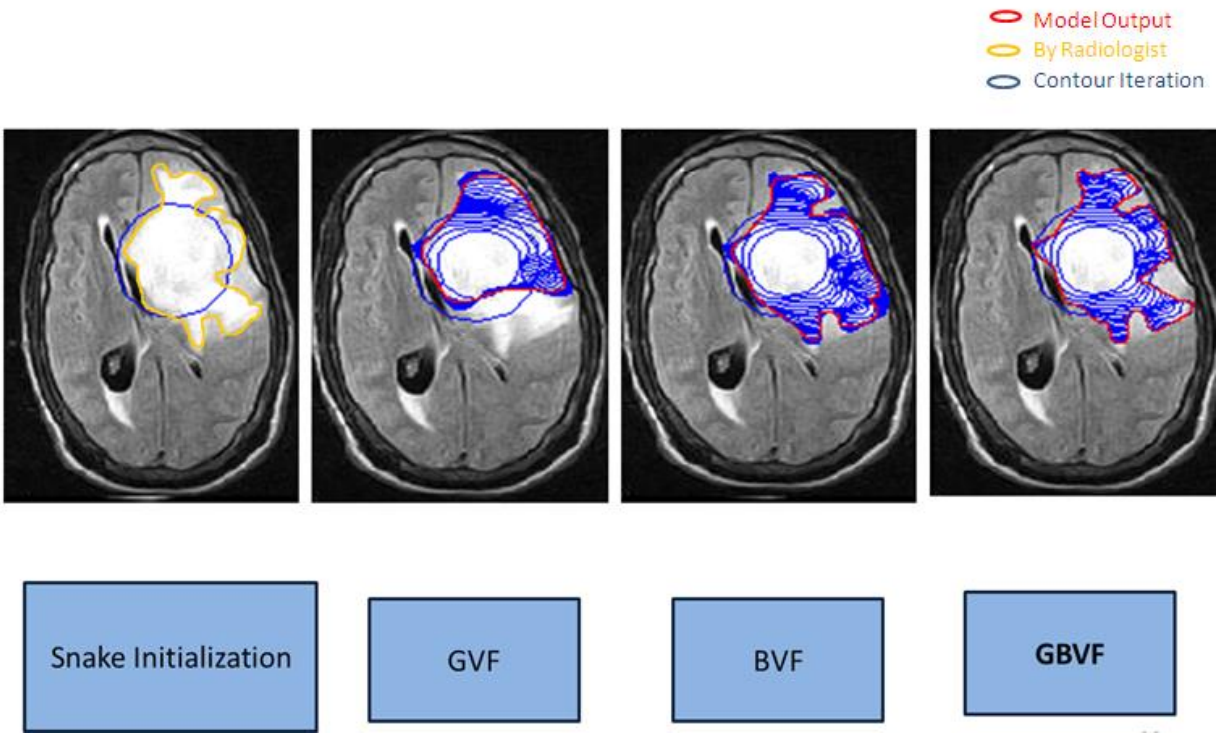

Figure 1: Comparative segmentation on head MR left parietal mass with contralateral subfalcine herniation, mass effect on flair image using (a) original image with initial snake in blue (b) processed with GVF, (c) processed with BVF, and (d) processed with GBVF deformable model. Yellow— ground truth marked by the radiologist; Blue— snake iteration; Red — output boundary extracted by different methods.

This tumor has complex shape, irregular boundary and acute concavities as shown in figure 1. Owing to limited capture range and presence of blurring edges GVF could not segment the tumor boundary accurately. BVF failed due to false edge detection so ended in preconvergence. While GBVF model precisely converged into the boundary concavities.

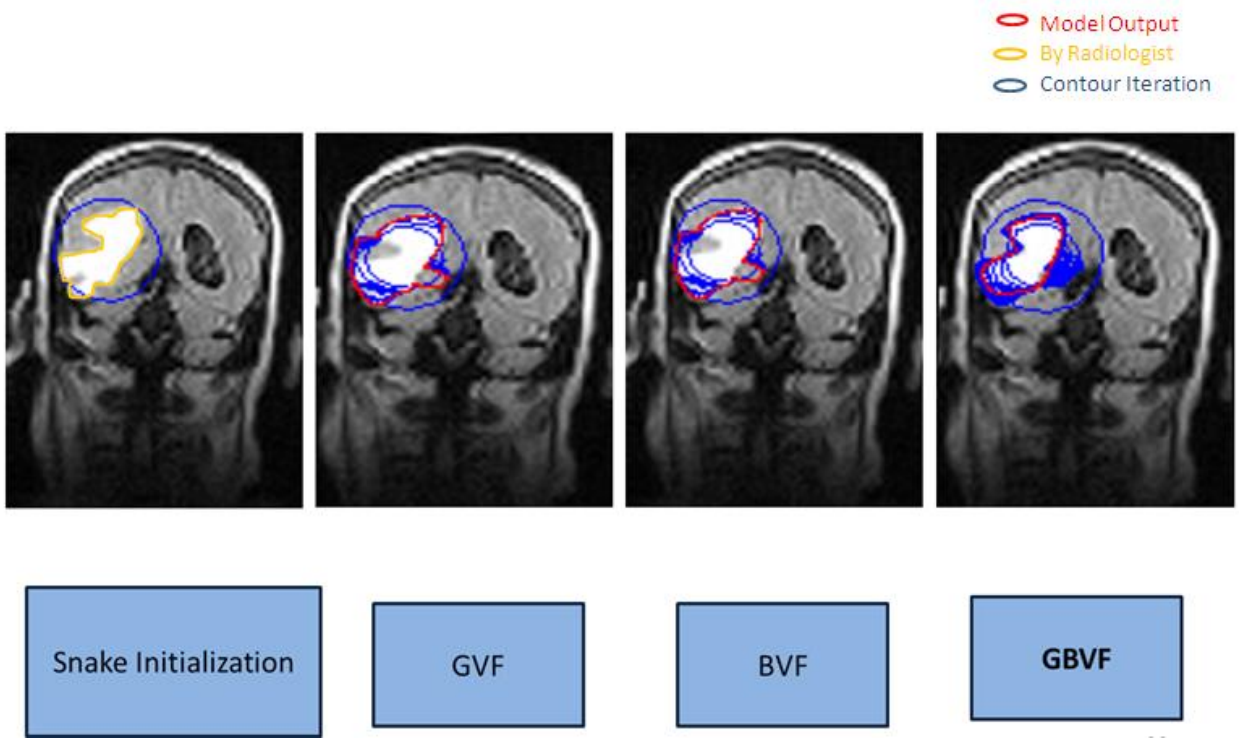

Figure 2: Comparative segmentation results on right high parietal para saggital hyperintense mass without significant mass effect T2-weighted image using (a) original image with initial snake in blue (b) processed with GVF, (c) processed with BVF, and (d) processed with GBVF deformable model... Yellow— ground truth marked by the radiologist; Blue— snake iteration; Red — output boundary extracted by different methods.

From the fig. 2(b) it is observed that the GVF snake is unable to evolve in the interior and cannot meet to boundary. This issue arises due to GVF deformable model trying to evolve in the vertical direction as central region has small effect of horizontal force. Observation shows GVF meets, if the initialization is closer to the boundary as shown in fig 2(c). In contrast, the GBVF deformable model meets to the boundary concavities as demonstrated in fig 2(d). Thus is concluded that the GBVF model is computationally less expensive and most robust to initialization.

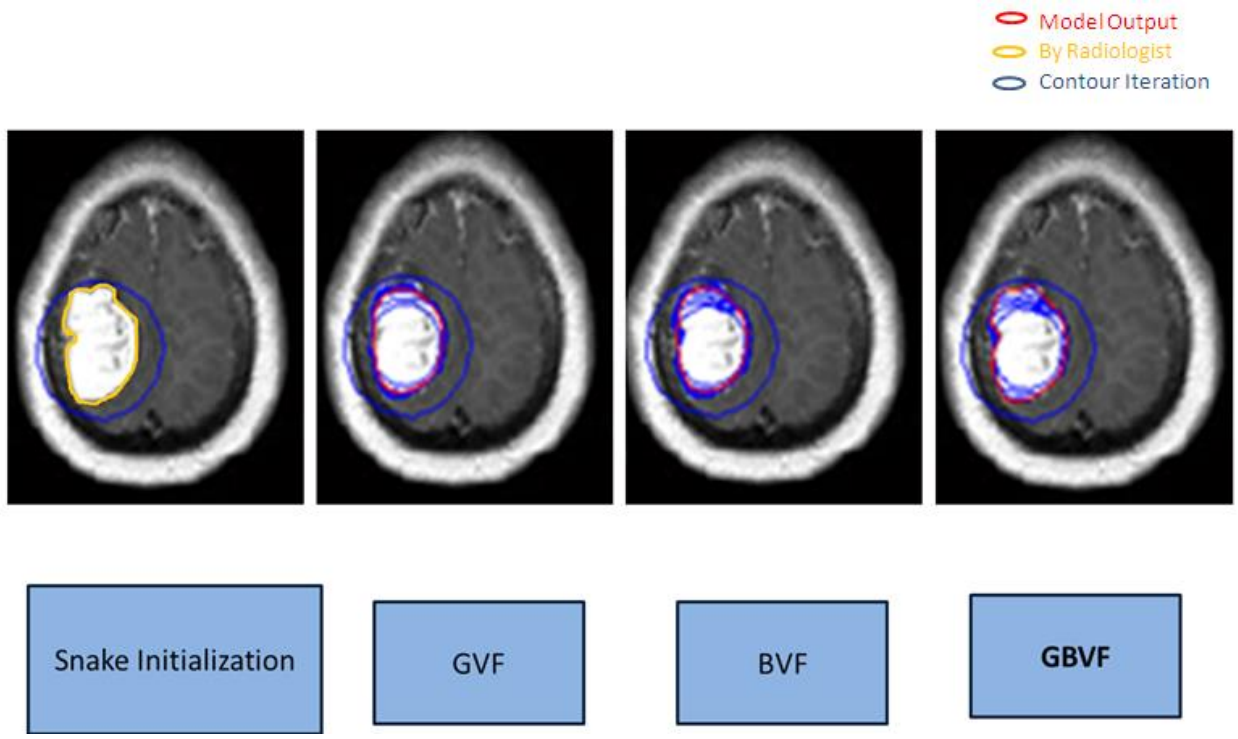

Figure 3: Comparative segmentation results on hyperintense rounded right high parietal mass using (a) original image with initial snake in blue (b) processed with GVF, (c) processed with BVF, and (d) processed with GBVF deformable model. Yellow— ground truth marked by the radiologist; Blue— snake iteration. Red — output boundary extracted by different methods.

Manual segmentation is evaluated in contrast to all three ACMs. GVF not succeeded to develop in the course of sporadic structures and distorted to the nearest edge. BVF also stepped across to the closest region as it could not identify the minor distinction between the gray matter and tumor intensity. Segmentation through BVF particularly needs closed binary boundary, which observed tricky to achieve in this specific image. Thus it leaked through irregular edges and remained unsuccessful to identify the tumor boundary. GBVF showed better behavior in extracting such complicated shaped tumor as it could evolve throughout the uneven boundary with sharp concavities.

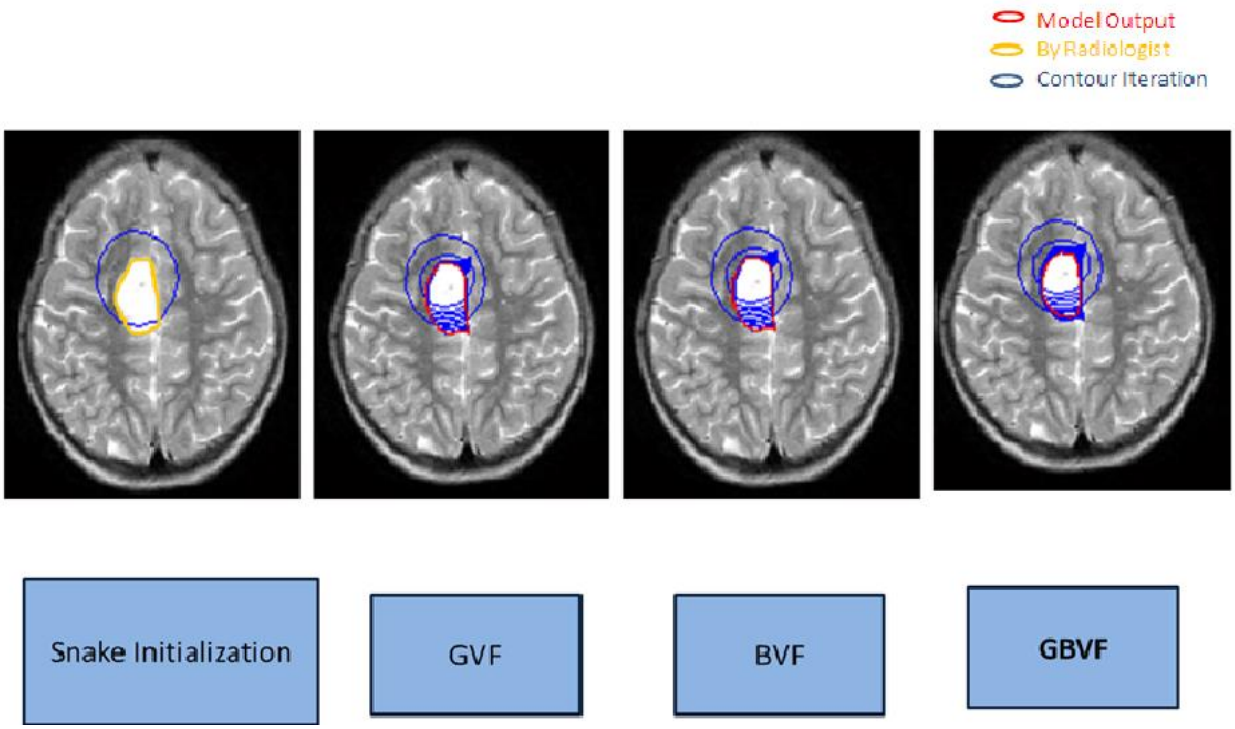

Figure 4: Comparative segmentation results on right high parietal para saggital hyperintense mass without significant mass effect T2-weighted image using (a) original image with initial snake in blue (b) processed with GVF, (c) processed with BVF, and (d) processed with GBVF deformable model. Yellow— ground truth marked by the radiologist; Blue—snake iteration. Red—output boundary extracted by different methods.

The GVF, BVF and GBVF deformable models were implemented to head MR T2-weighted image right high parietal para saggital hyperintense mass without significant mass effect and comparison among them was carried out. The original image is as shown in fig 4(a) with initial contour and results of segmentation are shown as (b) GVF segmentation; (c) BVF segmentation; (d) GBVF segmentation. In this tumor case all three ACMs somehow succeeded in extracting tumor boundaries. However GBVF comparatively gives better result.

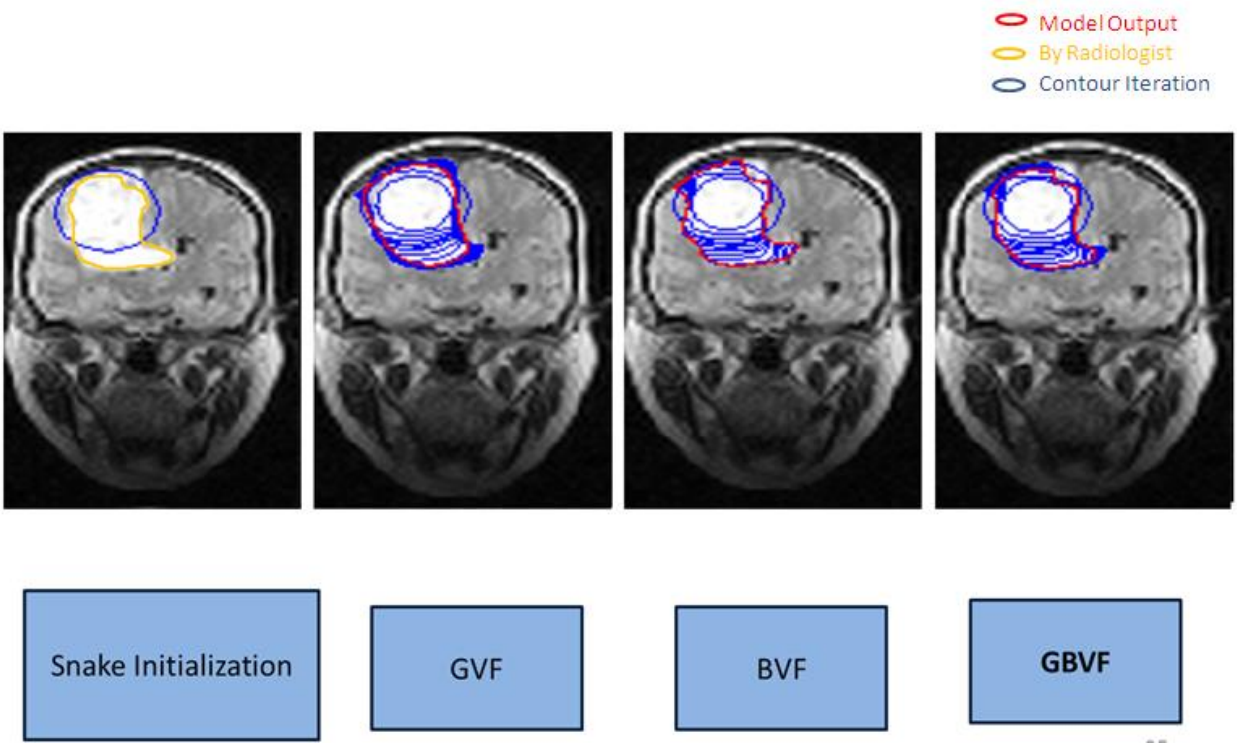

Figure 5: Comparative segmentation results on flair coronal meningioma; appearance, homogeneous tumor with isointense signal using (a) original image with initial snake in blue (b) processed with GVF, (c) processed with BVF, and (d) processed with GBVF deformable model. Yellow— ground truth marked by the radiologist; Blue— snake iteration; Red — output boundary extracted by different methods.

Figure 5 demonstrates comparative segmentation result on a homogeneous meningioma tumor having well-defined edges. This is the case of hyperintense tumor-uniform intensity in tumor's content but different intensity from gray matter. In this case, GVF and BVF finely segment the tumor due to high contrast, the difference between the tumor boundary and the background. GBVF also shows smoother boundary extraction.

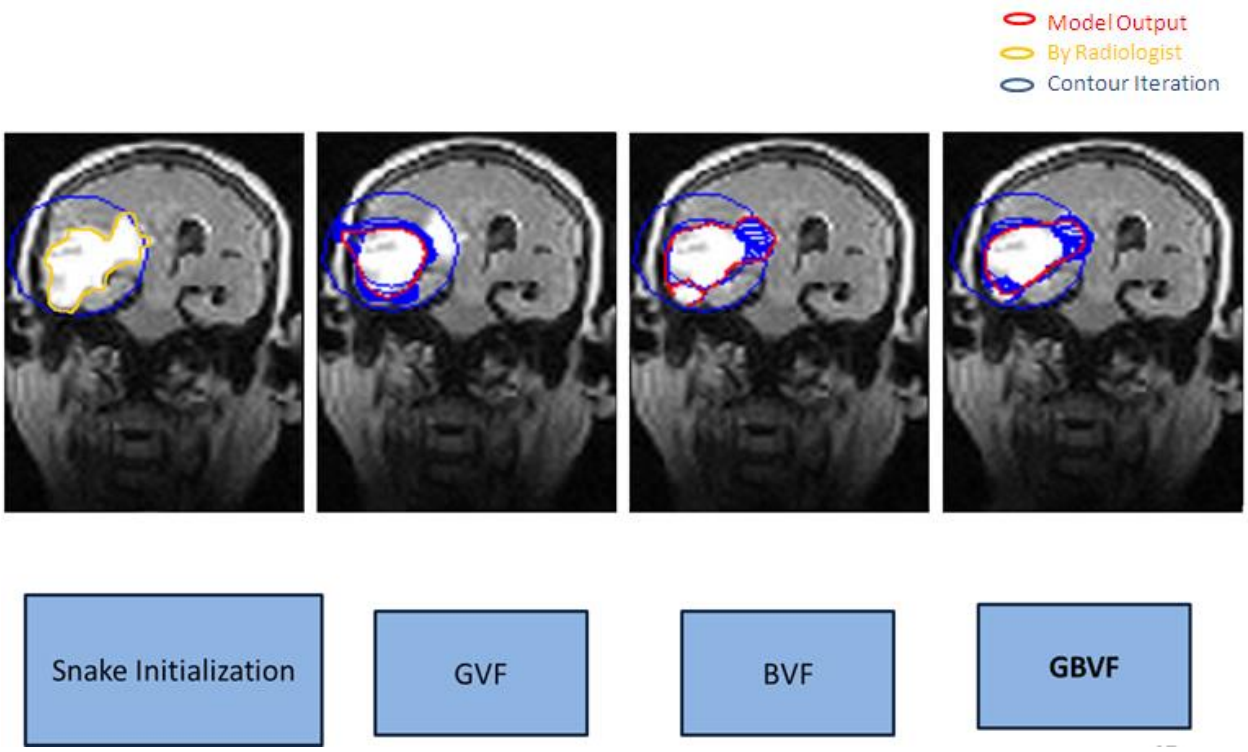

Figure 6: Comparative segmentation results on T1 coronal showing hyperintense mass with contralateral subfalcine herniation & shift using ((a) original image with initial snake in blue (b) processed with GVF, (c) processed with BVF, and (d) processed with GBVF deformable model. Yellow— ground truth marked by the radiologist; Blue— snake iteration; Red — output boundary extracted by different methods

The GVF, BVF and GBVF ACMs were applied on Head MR T1 coronal weighted images showing hyperintense mass with contralateral subfalcine herniation & shift and comparison among them was carried out against manual segmentation done by radiologist. The original image is as shown in figure 6(a) and results of segmentation of using GVF, BVF and GBVF models are as shown in figure 6 (b), 6 (c) and 6 (d) respectively. The GVF deformable model could not segment the real boundaries; since the directional force growing towards the desired boundary is weaker as compare to local noise. The GVF ACM also tends to move to the outer region of the tumor in addition to the desired edges. BVF also failed to detect correct boundary. This problem was overcome by using GBVF deformable model.

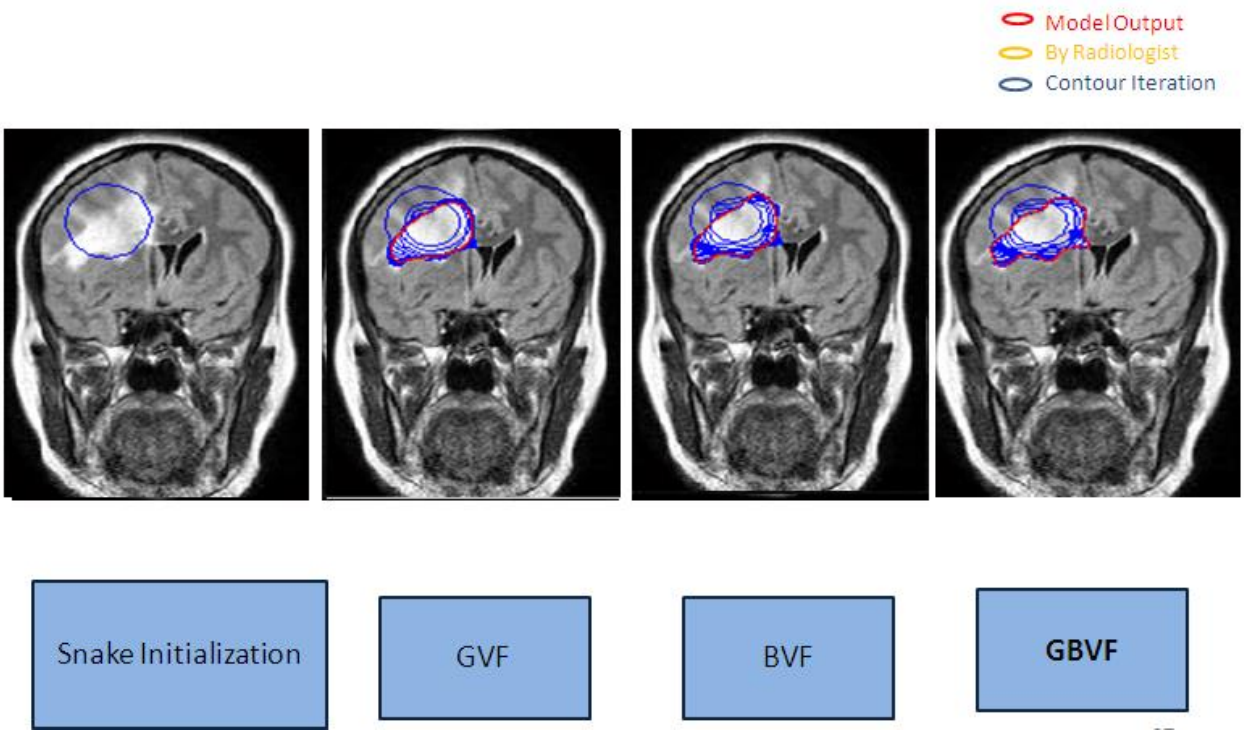

Figure 7: MR T1 weighted coronal image with huge hyperintense mass causing contralateral subfalcine herniation. Compression of ipsilateral lateral ventricle a) Initial contour marked in image (b) Processed with GVF deformable model, (c) Processed with BVF deformable model, (d) Processed with GBVF deformable model. Yellow— ground truth marked by the radiologist; Blue— snake iteration; Red— Output Boundary.

The segmentation of tumor on head MR image was carried out using GVF, BVF and GBVF models. The segmented results were compared with the manual segmentation in terms of boundary of tumor. 7(a) shows the original image with snake initialization and its results of segmented image using GVF, BVF and GBVF are as shown in fig 7(b), 7(c) and 7(d) respectively. From the results, it is concluded that the GVF not succeeded to move in the course of sporadic structures and distorted to the nearest edge. BVF also stepped across to the closest region as it could not identify the minor distinction between the gray matter and tumor intensity. This issue was overcome by GBVF.

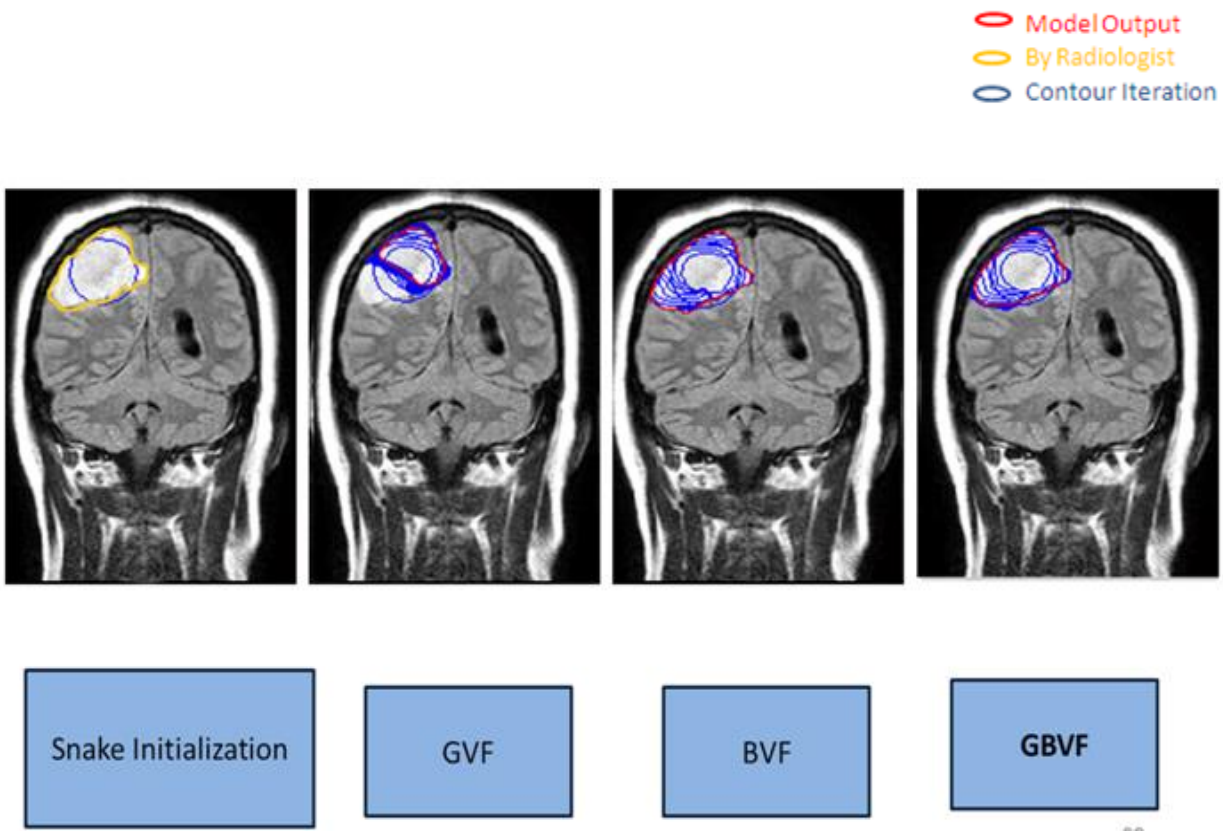

Figure 8: (a) Original image of coronal flair image hyperintense mass with mild contralateral mid line shift & mass effect with initial contour (b) Processed with GVF deformable model, (c) Processed with BVF deformable model (d) Processed with GBVF deformable model. Yellow— ground truth marked by the radiologist; Blue— snake iteration. Red — output boundary extracted by different methods.

In this figure contour is initialized inside the tumor. Here coronal flair image hyperintense mass with mild contralateral mid line shift & mass effect with initial contour is shown in (a) ,three ACMs are shown in (b) GVF, (c) BVF and (d) GBVF. The manual segmentation is compared against three ACMs .Results Show that the GVF snake does not converge at all due to the static equilibrium force field. BVF and GBVF can extract the boundary of this object.

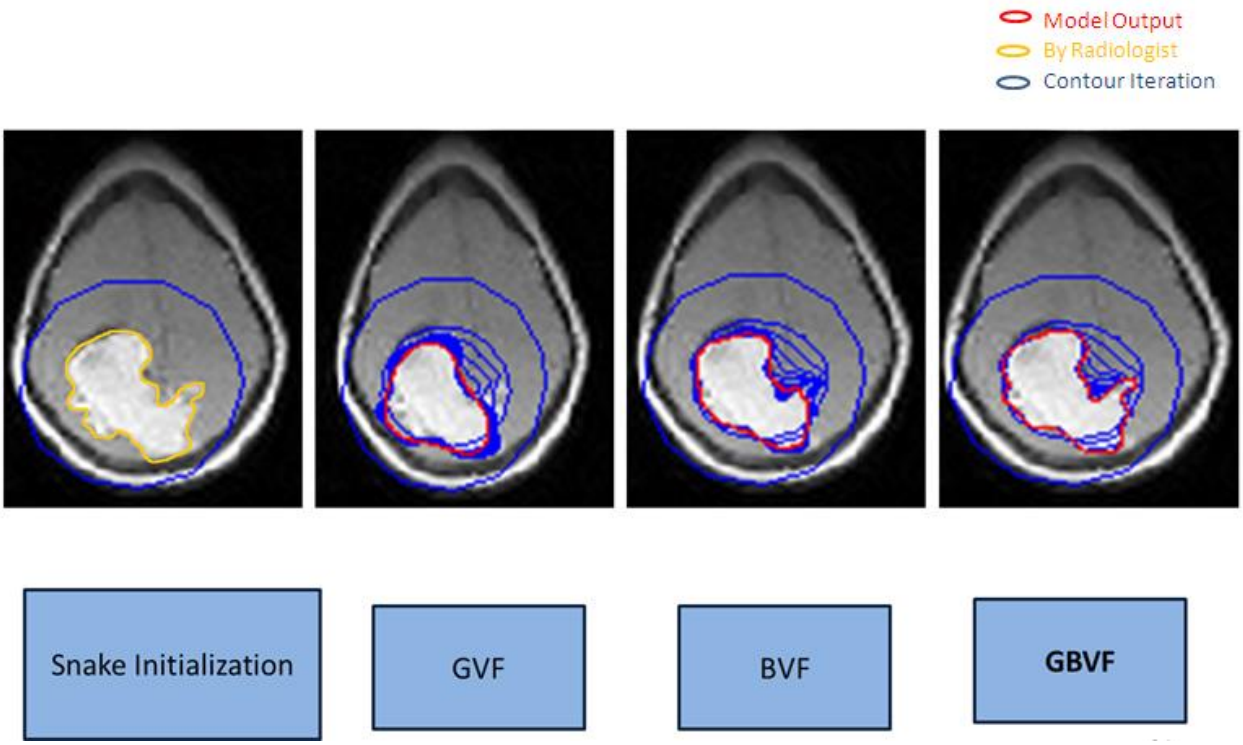

Figure 9: Comparative segmentation results on T1 axial irregular hyperintense mass with contra lateral extension high parietal region using (a) original image with initial snake in blue (b) processed with GVF, (c) processed with BVF, and (d) processed with GBVF deformable model. Yellow— ground truth marked by the radiologist; Blue— snake iteration; Red —output boundary extracted by different methods.

GVF have upward vectors around the bottle neck of the concave region. These upward vectors block the way of the snakes to move onto the concave region. In contrast, BVF provides strong downward vectors which are ascribed by the boundary interpolation scheme. And GBVF can extract the true boundary of this tumor. They are able to distinguish positive boundary from negative boundary and works better than the GVF deformable model.

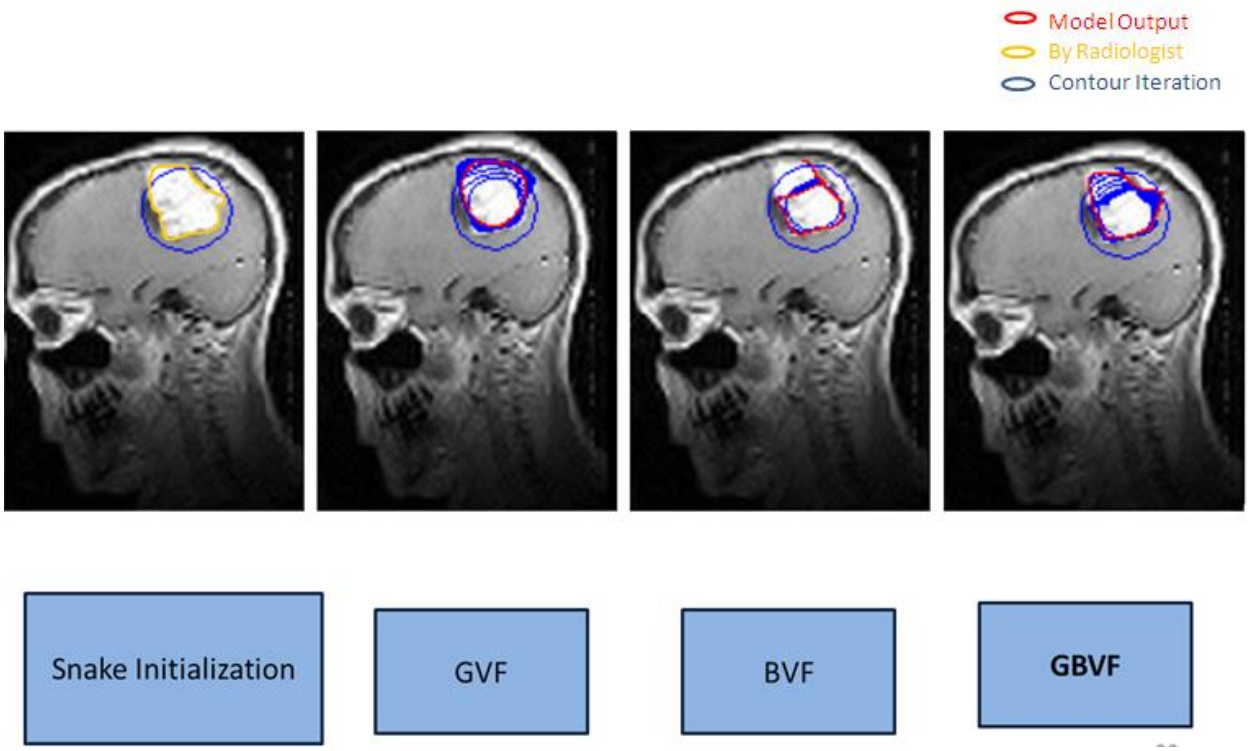

Figure 10: (a) original image with initial snake in blue (b) processed with GVF, (c) processed with BVF, and (d) processed with GBVF deformable model .Yellow— ground truth marked by the radiologist; Blue— snake iteration. Red — output boundary extracted by different methods.

Manual segmentation is compared against all these methods. The snake boundary travels in the radial direction defined by GVF motion field, which is unable to segment complex-shaped objects. GVF stepped across the irregular edges and failed to localize the tumor boundary. BVF failed to extract true tumor boundary. GBVF evolved through the irregular boundary with acute concavities and gives superior performance in segmenting such complex shaped tumor.

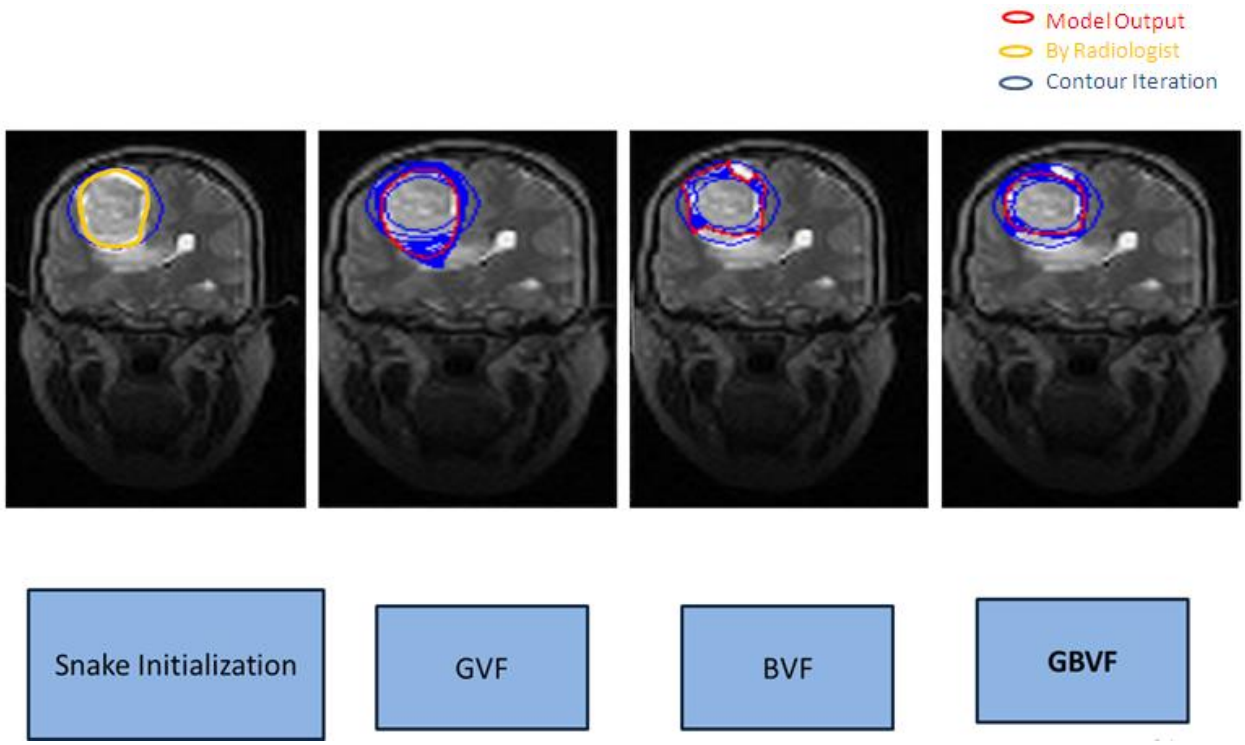

Figure 11: Comparative segmentation results on right high parietal para saggital hyperintense mass without significant mass effect T2-weighted image using (a) original image with initial snake in blue (b) processed with GVF, (c) processed with BVF, and (d) processed with GBVF deformable model Yellow— ground truth marked by the radiologist; Blue— snake iteration; Red — output boundary extracted by different methods.

Manual segmentation is compared against all these methods. Limited capture range — the GVF vector field is static and independent of the initial contour marked. If GVF contour is not initialized at the center of the target, GVF field acts on all elements of contour along same direction and results in its collapse to a portion of boundary and, therefore, is unable to cover the whole Tumor. GBVF evolved through the irregular boundary with acute concavities and gives superior performance in segmenting such complex shaped tumor.

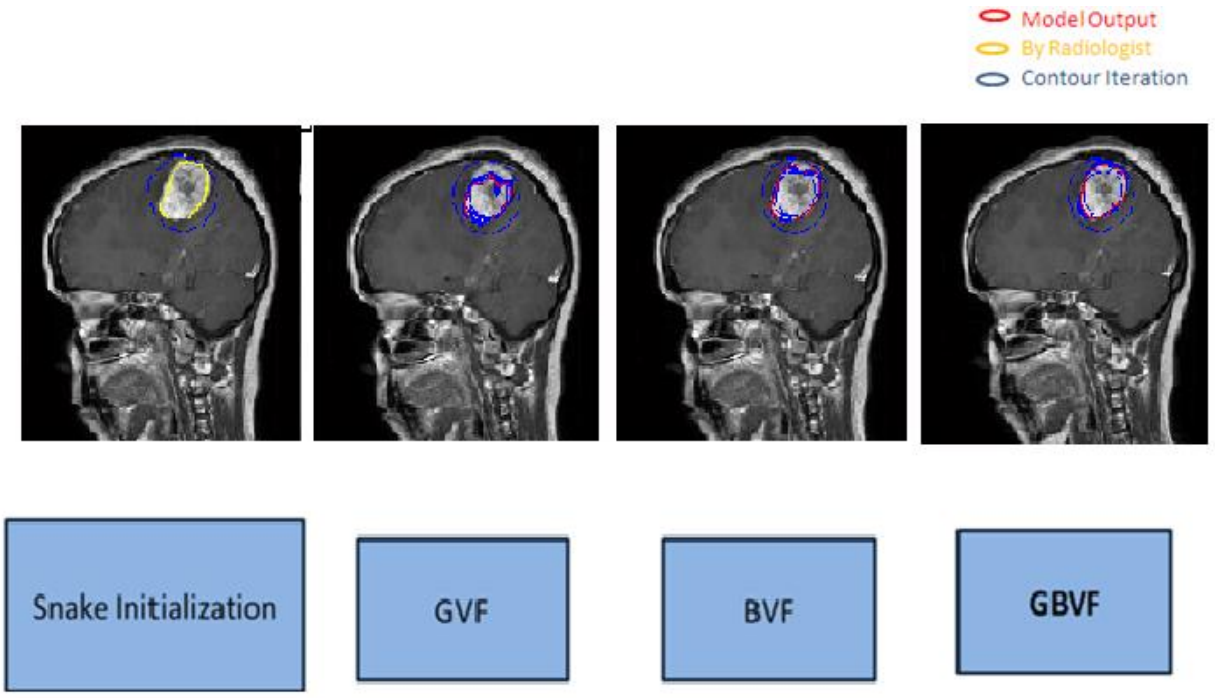

Figure 12: Comparative segmentation results on T2 weighted saggital image showing oval shaped hyperintense mass in parietal region with internal hypointensities using (a) original image with initial snake in blue (b) processed with GVF, (c) processed with BVF, and (d) processed with GBVF deformable model. Yellow— ground truth marked by the radiologist; Blue— snake iteration. Red — output boundary extracted by different methods.

We can see that the GVF snake does not evolve at all. . The GVF ACM could not segment the real boundaries; since the directional force growing towards the desired boundary is weaker as compare to local noise. BVF also failed to extract true boundaries. While GBVF successfully found true boundaries.

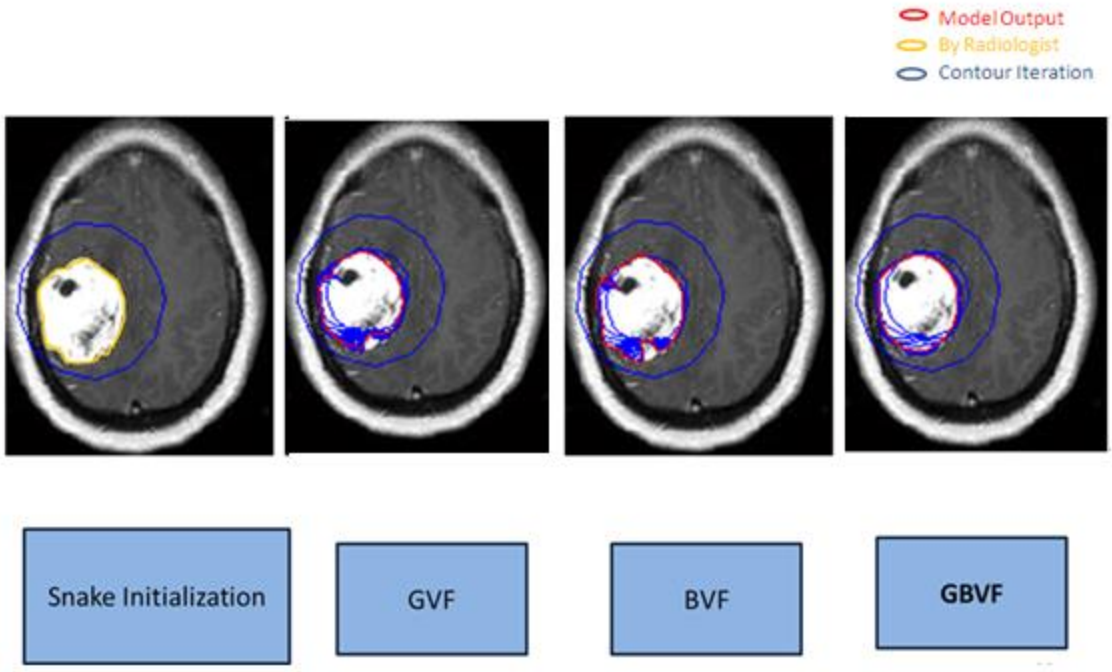

Figure 13: Comparative segmentation results on T2 axial image hyperintense mass right parietal region with mild mass effect using (a) original image with initial snake in blue (b) processed with GVF, (c) processed with BVF, and (d) processed with GBVF deformable model. Yellow—ground truth marked by the radiologist; Blue— snake iteration; Red— output boundary extracted by different methods.

Figure 13 demonstrates comparative segmentation result results on T2 axial image hyperintense mass right parietal region with mild mass effect. (a) GVF, (b) BVF, and (c) GBVF.

Since tumor is not homogeneous with interim pseudo edges so GVF could not extract exact tumor boundary. GVF not succeeded to move in the course of sporadic structures and distorted to the nearest edge because of the preconvergence problem — converged at false edges and local minima. BVF partially succeeded but GBVF showed much better result than other two ACMs

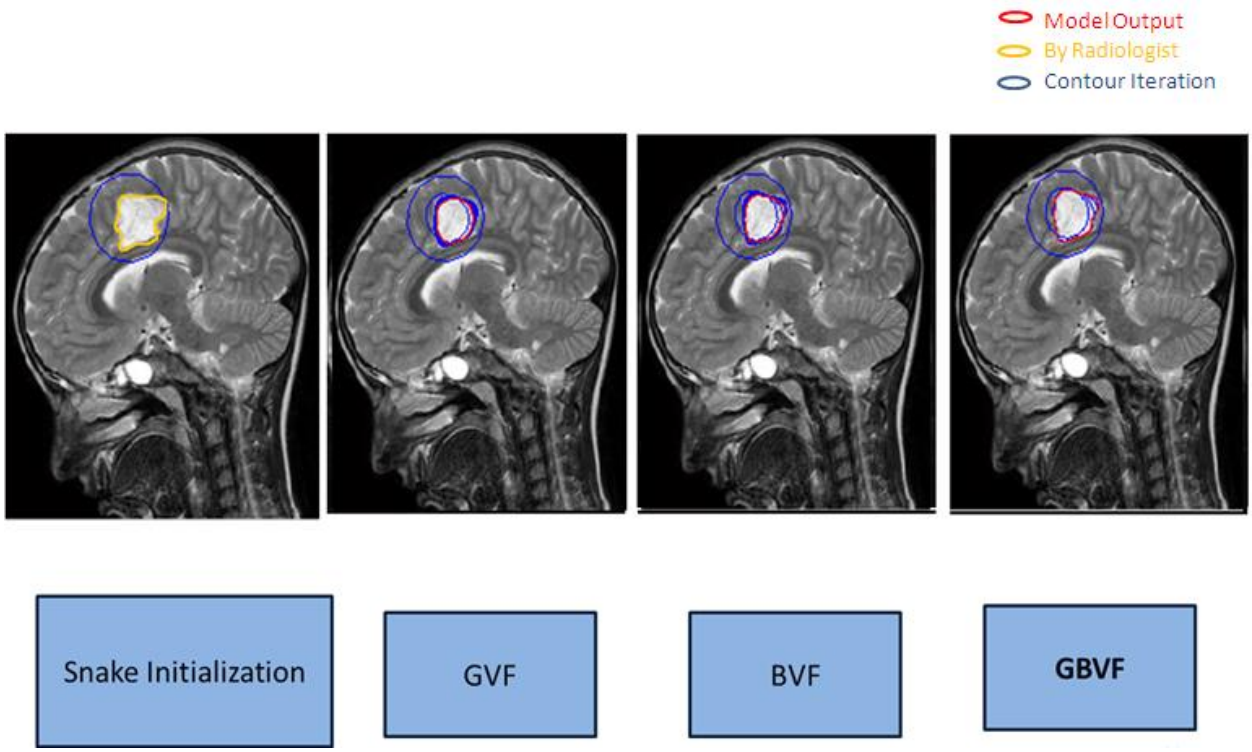

Figure 14: (a) Original saggital T2 - weighted image with initial contour, (b) Processed with GVF deformable model, (c) Processed with BVF deformable model, (d) Processed with GBVF deformable model. Yellow— ground truth marked by the radiologist; Blue— snake iteration; red — output boundary extracted by different methods.

The GVF, BVF and GBVF ACMs were applied on Head MR T2 - weighted image (a) shows original image with initial contour (b) shows GVF active contour model (c) BVF active contour model (d) GBVF active contour model. It is observed that the GVF snake is unable to evolve in the interior and cannot meet to exact boundary. BVF also failed to extract true boundaries, while in this case GBVF is somehow able to converge into tumor boundary

Chapter 4

Discussions and Conclusions

4.1 Discussion

Medical image processing and analysis are challenging research areas. In order to ensure the accuracy, efficacy, and repeatability of processing complicated medical images, advanced image processing techniques are always in needs to improve the procedures. Image segmentation is the most fundamental image processing techniques and is vital in many practical image analysis tasks[24, 25, 26, 27]. In this research works, Active contour methods in image processing are studied. They include Gradient Vector Flow, Boundary Vector field, and Generalized Vector Boundary field. The contribution of this research is on active contour models. Active contour or snake is a well defined image segmentation tool and is proven to be useful in many medical image processing tasks [28, 29, 30, 31]. The effectiveness of ACMs is basically governed by its overall energy functional. In Chapter 2 methodology of traditional snake as well as three ACMs: Gradient Vector flow GVF, Boundary Vector Field BVF and Generalized Boundary Vector Field GBVF is explained. Then computational setup and parameter selection and setting is discussed in addition to different methods of snake initialization. Due to the various challenges posed by the medical images, in terms of extracting the actual boundary of the target object within a given image, the various deformable contour methods studied in this paper showed their versatility and shortcomings. It is concluded that even though there are still many challenges to be faced, it is with a better understanding of both the problems and the features provided by the various methods that a successful solution could be devised.

First, GBVF provides ultimate capture range. The initial contour can be placed as far as the border of the image; GBVF can still evolve towards to the target tumors easily. Second, the capability of extracting concave tumor is better than GVF. In additional to the simple concave tumors, the complex concave tumors can also be extracted in a fast-pace manner. Third, BVF and GBVF is generated by robust interpolation scheme while another comparable external force, GVF, is generated by a slow diffusion process. Thus, the computation requirement of the BVF and GBVF is extremely low.

4.2 Conclusions

The complexity and variability of brain tumor anatomic structures, poses many challenging problems for image processing community in search for a good segmentation model. The main goal of this project was to compare three different methods within the active contour framework to extract brain tumor boundary. Experiments are performed to analyze the working of three ACMs: GVF, BVF and GBVF. These were analyzed in detail and implemented in MATLAB. The three snake models were then tested on some typical cross-sectional views of a number of different brain tumors MR images to highlight the conditions required in order to have the snakes perform satisfactory. The experimental results also made it possible to closely compare the performance of each snake model. All in all the main goal of the project, to compare three different ACMs, has been fulfilled. In the experimental results section it was established that under most conditions an ACMs can perform satisfactory, but in images with boundary concavities problems can occur . Based on the research works discussed above, it is shown that ACMs are efficient and flexible for advanced image processing, and particularly in the applications of brain tumor segmentation. It was also established that the strength of ACMs is that they are versatile and can fit a great number of different shapes. GBVF has shown

substantial results in extracting complex concave tumor boundaries as compare to GVF and BVF. Of weaknesses can be mentioned the fact that the parameters of the snake has to be adjusted manually.

References

[1] Z. H. Cho, J. P. Jones, and M. Singh, Foundations of Medical Imaging. New York: Wiley, 1993.

[2] T. McInerney and D. Terzopoulos, \Deformable models in medical image analysis: A survey," Medical Image Analysis, vol. 1, no. 2, pp. 91-108, 1996.

[3] T. F. Chan and L. A. Vese, \Active contours without edges," IEEE Trans. Image Processing, vol. 10, no. 2, pp. 266-277, 2001.

[4] R. Grzeszczuk, D. Levin, ‘‘Brownian strings’’: segmenting images with stochastically deformable contours, IEEE Trans. Anal. Machine Intell. 19 (1997) 1100–1114.

[5] L.H. Staib, J.S. Duncan, Boundary finding with parametrically deformable models, IEEE Trans. Pattern Anal. Machine Intell. 14 (1992) 1061–1075.

[6] T. Wang, I. Cheng, and A. Basu, “Fluid Vector Flow and application in Brain Tumor segmentation”, IEEE TBME, 2009 56(3):781-789

[7] T.F. Cootes, A. Hill, C.J. Taylor, J. Haslam, Use of active shape models for locating structures in medical images, Image Vis. Comput.12 (1994) 355–366

[8] L. Cohen, on active contour models and balloons, CVGIP Image
Understand. 52 (2) (1991) 211–218.

[9] Sanaz Rahimi, Mehdi R. Zargham, Jie Cheng: A Method to Detect, Locate and Mark Brain Tumors. IPCV 2010: 564-567

[10] T.F. Chan, L.A. Vese, Active contour without edges, IEEE Trans.Image Process. 10 (2001) 266–277.

[11] Alejandro Veloz, Steren Chabert, Rodrigo Salas, Antonio Orellana, Juan Vielma:Fuzzy Spatial Growing for Glioblastoma Multiforme Segmentation on Brain Magnetic Resonance Imaging. CIARP 2007: 861-870

[12] T. McInerney, D. Terzopoulos, T-snakes: topologically adaptive snakes, Med. Image Anal. 4 (2) (2000) 73–91.

[13] A. Lundervold, G. Storvik, Segmentation of brain parenchyma and cerebrospinal fluid in multispectral magnetic resonance images, IEEE Trans. Med. Imaging 14 (1995) 339–349.

[14] M. Kass, A. Witkin, and D. Terzopoulos, \Snakes active contour models, "International Journal of Computer Vision, pp. 321-331, 1988.

[15] Chenyang Xu and Jerry L. Prince, "Snakes, Shapes and Gradient Vector Flow," IEEE TIP, 1998, 7(3): 359-369.

[16] K.W.Sum and P.Y.S. Cheung, "Boundary Vector field for Parametric Active Contours," PR, 2007, 40(6): 1635-1645.

[17] K. W. Sum and Paul Y. S. Cheung, "A Fast Parametric Snake Model with Enhanced Concave Object Extraction Capability" IEEE, 2006.

[18] B. Ostlad, A. Tonp, Encoding of a priori information in active contour models, IEEE Trans. Pattern Anal. Machine Intell. 18 (9) (1996) 863–872.

[19] S.D. Fenster, J.R. Kender, Sectored snakes: evaluating learned energy segmentations, IEEE Trans. Pattern Anal. Machine Intell. 23 (9) (2001) 1028–1034.

[20] X. Wang, L. He, W.G. Wee, Deformable contour method: a constrained optimization approach, Int. J. Comput. Vis. 59 (1) (2004) 87–108.

[21] R. & Martín-Landrove, M. (2006). Brain Tumor Image Segmentation Using Neural Networks, Proceedings 14th Scientific Meeting International Society for Magnetic Resonance in Medicine, ISBN 1522-2594, Seattle-Washington-USA, May 6-12, 2006

[22] Yang, J.; Zhang, Z. & Zhu, Y. (2005). Semi-automated brain tumor and edema segmentation using MRI. European Journal of Radiology, Vol.56, No.1, (October 2005), pp. 12-19, ISSN 0720-048X

[23] Xu, J. & Zhao, H. (2003). An Eulerian Formulation for Solving Partial Differential Equations along a Moving Interface. Journal of Scientific Computing, Vol.19, No.1–3, (December 2003), pp. 573-594, ISSN 0885-7474

[24] Zhang, Y.; Brady, M. & Smith S. (2001). Segmentation of brain MR images through a hidden Markov random field model and the expectation-maximization algorithm. IEEE Transactions on Medical Imaging, Vol.20, No.1, (January 2001), pp. 45-57, ISSN 0278-0062

[25] K. Siddiqi, Y.B. Lauzie`re, A. Tannenbaum, S.W. Zucker, Area and length minimizing flows for shape segmentation, IEEE Trans. Image Process. 7 (3) (1998) 433–443

[26] Medical Image Processing Overview Hongmei Zhu, University of Calgary

[27] F. Leymarie and M. D. Levine, \Tracking deformable objects in the plane using an active contour models," IEEE Trans. Pattern Analysis and Machine Intelligence, vol. 15, no. 6, pp. 617-634, 1993.

[28] J. Tohka, Surface extraction from volumetric images using deformable meshes: a comparative study, in: Proceedings of the Seventh European Conference on Computer Vision (ECCV), 2002, pp. 350–364.

[29] A.F. Frangi, W.J. Niessen, M.A. Viergever, Three-dimensional modelling for functional analysis of cardiac images: a review, IEEE Trans. Med. Imaging 20 (1) (2001) 2–25.

[30] H. Delingette, J. Montagnat, Shape and topology constraints on parametric active contours, Comput. Vis. Image Understand. 83 (2001) 140–171.

[31] C. Xu, D.L. Pham, J.L. Prince, Medical image segmentation using Deformable models, in: SPIE Handbook on Medical Imaging – vol. III: Medical Image Analysis, May 2000, pp. 129–174.